

**ALPHA FOUNDATION AFC518-2  
FINAL REPORT**

**1.0 Cover Page:**

**Grant Number and Title:** AFC 518-2, Miniaturized and Real Time Gas Sensors for Mine Safety and Health

**Organization Name:** Oakland University

**Principle Investigator:** Xiangqun Zeng

**Contact Information (email, phone, fax) :**

e-mail : [zeng@oakland.edu](mailto:zeng@oakland.edu); Tel : 248-370-2881; Fax: 248-370-2321.

**Period of Performance:** Sept. 1, 2017 to Feb. 28, 2019

**Acknowledgement/Disclaimer:**

This study was sponsored by the Alpha Foundation for the Improvement of Mine Safety and Health, Inc. (ALPHA FOUNDATION). The views, opinions and recommendations expressed herein are solely those of the authors and do not imply any endorsement by the ALPHA FOUNDATION, its Directors and staff.

## 2.0 Executive Summary

Despite improvements in safety measures, mine workers continue to experience risks from hazardous gases. Real-time and continuous-use portable gas sensors are needed for monitoring explosive and/or toxic gases in the dynamic mine environment for the safety and health of mine workers. Although there are many gas monitoring systems commercially available, none of them is capable of the real-time, continuous measurement of gas concentrations within an individual miner's local environment needed to assess personal exposure and risk. We have pioneered a ***new gas sensor technology*** utilizing ionic liquids (ILs) that provides an optimal solution for ambient gas monitoring. Our IL electrochemical gas sensor (IL-EG) is particularly attractive in mine applications because ILs are non-volatile and non-flammable, and therefore permissible for use in extreme operating conditions such as those routinely present in mine environments. An ideal sensor for mine safety applications would be compact, inexpensive, portable, and have low power requirements – but could provide continuous monitoring of multiple hazardous gas concentrations. Our new sensor technology has the potential to satisfy all of these requirements; but to do so, we first need to address several major technical challenges, i.e. sensor miniaturization, sensor sensitivity, selectivity and sensor stability (signal drift). It was possible that sensor sensitivity could be compromised due to sensor miniaturization; sensor selectivity and stability could be affected due to changes in the sensing environment (e.g. temperature, humidity variations) routinely encountered in mines.

Supported by our AFC518 award, we carried out proof-of-concept research addressing those difficulties. Our preliminary work had two research objectives: 1. *Sensor chip miniaturization*; and 2. *Miniaturized gas sensor characterization and validation for accurate and reliable measurements in regard to confounding factors such as temperature and humidity variations in mining environments*. Two complementary types of miniaturized gas sensor devices were designed, fabricated and tested to demonstrate the technological readiness of the concept to continue toward prototype development. One type was a miniaturized planar electrochemical sensor using ionic liquids as electrolytes and solvents. The other was a tuning fork piezoelectric gas sensor that detected methane with good selectivity and sensitivity. Both miniaturized sensor platforms can be integrated for multimodal and multi-gas detection. The sensors were tested for oxygen, hydrogen and methane (selected for their relevance to mine safety) detection at varying temperature and humidity levels.

Our progress is highlighted in four complete manuscripts/publications listed below and details are shown in section 3. In the appendix, we also briefly summarize our on-going work. Our results have proven the feasibility of our innovative microsensor prototypes and also contributed to increased scientific knowledge of mechanisms of sensing reactions and sensor performance in conditions similar to those prevailing in mine environments that are not reported in the literature. These accomplishments establish the feasibility and technological readiness of our gas sensor technology for the next phase of research: development and optimization for field-testing, validation and commercialization.

1. Effects of Water on Ionic liquid Electrochemical Microsensor for Oxygen Sensing Sensors & Actuators: B. Chemical, **2019**, 285, 350-357. ***Key results***: *sensor long-term stability can be obtained in the presence of water at ionic liquid microsensor device.*
2. Quartz tuning fork (QTF) based methane sensor for coal mine safety application, Sensors & Actuators: B. Chemical, In revision. ***Key-results***: *QTF methane sensor achieved a detection limit of 0.025% methane with good selectivity to CO<sub>2</sub>.*
3. Platinum-nickel (Pt-Ni) bimetallic nanosphere and ionic liquid as sensing interface for electrochemical oxygen and hydrogen sensors, ACS Applied Nano Materials, In revision. ***Key results***: *Integrating ionic liquid (electrolyte) and nanomaterial (electrode) enables electrocatalysis for high performance inexpensive microsensor development for multiple gases detection.*
4. A redox conjugated polymer-based all-solid-state reference electrode, Polymers, **2018**, 10, 1191. ***Key results***: *a new class of all-solid-state reference electrode that can be implemented in various electrochemical micro-devices.*

### 3.0 Concept Formulation and Mission Statement

Mine workers continue to experience risks from hazardous gases, as evident from the numerous reports of injuries and health related issues linked to gas explosions and toxic gas emissions. While great progress has been made in promoting worker safety and health, the need for better gas sensing technology is readily apparent. Several types of atmospheric monitoring systems (AMS) for hazardous gases and mine ventilation systems (MVS) exist; however, since they typically collect and/or analyze air samples only periodically, they fail to capture temporal and spatial variations of gas concentrations that occur in real time. Numerous attempts have been made to develop portable gas monitors or sensors, but most of the currently available portable gas monitors are expensive and bulky with poor spatial and temporal resolution (only a few sampling points across the mine). They are insufficient to capture the dynamics of hazardous mine gas emission and are inadequate for modeling and prediction purposes. Moreover, commercially available portable gas sensors developed for air pollution monitoring target different gaseous pollutants such as volatile organic compounds and automobile emissions. Mines have very different gaseous environments and ambient conditions, involving different types of gases and concentration ranges. Portable gas sensors developed for air quality monitoring are not directly adaptable for mine safety and health applications. Thus, no current portable gas sensor technology meets the challenging requirements needed for development of personal, continuous-use, multi-gas monitors for different work environments in mines.

Our mission is to develop miniaturized sensor technology to detect/sense and identify hazardous gases, chemicals, and conditions in mines through a multimodal orthogonal electrochemical and piezoelectric sensor approach. Our electrochemical approach exploits the unique electrochemistry and interface chemistry of ionic liquid (IL) sensing materials and well-established inexpensive, small size and low power electrochemical transducers to produce a miniaturized wearable electrochemical sensor that can simultaneously monitor multiple hazardous gases in mines with high reliability in real time. Our piezoelectric approach was dictated by the need to address methane detection safely and efficiently. Methane is an inert, colorless, odorless gas that is ubiquitous in coal mines, and normally requires either electrocatalysts or high temperatures for electrochemical detection. We therefore developed a piezoelectric methane sensor based on the resonating quartz tuning fork (QTF). The QTF approach is based on the fact that methane is lighter and less viscous than air, and thus the presence of methane will increase the QTF's resonant frequency. This type of methane sensor has very low cost, high stability, and an excellent selectivity to heavier gases such as CO<sub>2</sub>. The quartz tuning fork sensor will be integrated with the IL electrochemical sensor for a multimodal and multi-gas detection sensor system in Phase II. The combination of electrochemical gas sensor and complementary piezoelectric QTF sensor will significantly improve methane detection accuracy and reliability.

Our research in the AF 518 Phase I project centered on advancing and demonstrating the effectiveness of our gas sensor technology for use, adoption, and adaptation into practice with two objectives: *1. sensor miniaturization; 2. validation of sensor reliability in mine conditions (varying humidity and temperature) for accurate and reliable measurement of mine gases.* We anticipate, based on our initial findings, that our sensor chip will form part of a hand-held or credit-card-sized detection unit with full microelectronics compatibility, extremely small size, low power consumption, and low production costs. Further research in Phase II on the sensor and its integration with advanced microelectronics will continue improving the sensor system's performance. Our end goal is to create a multimodal sensor technology for highly reliable monitoring and evaluating multiple gaseous hazards in mines. Ultimately, we see our miniaturized gas sensors as a driver for autonomous/self-reporting distributed and networked applications to significantly impact mine safety and health.

### 4.0 Proof-of-Concept Technology Components

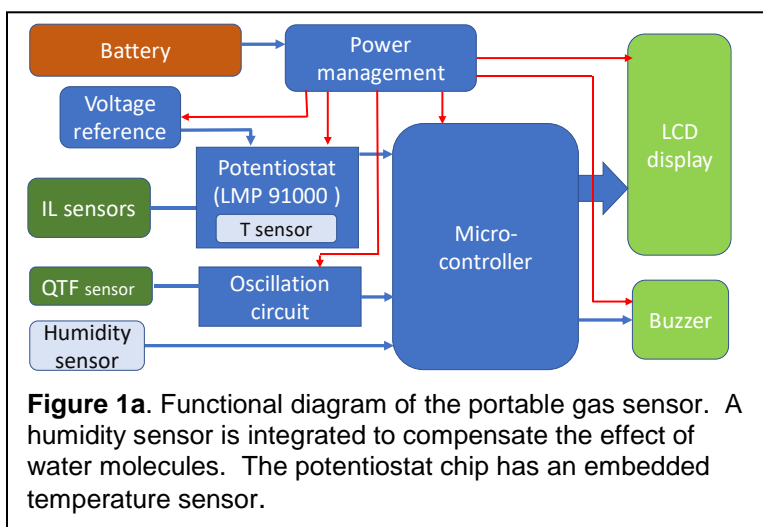
The ultimate goal of this project is to develop a battery-powered **Mine Gas Sensor System (MGSS)** that can be strategically distributed throughout a mine in fixed locations, on vehicles, or worn by miners

to monitor relevant gas concentrations. It is expected that the final device will have the following characteristics.

1. **Utility:** accurate measurement of all important mine gases in a single instrument.
2. **Wearability:** small, lightweight, battery powered for long durations.
3. **Practicality:** low cost, easy to install, reliable.
4. **Compatibility:** usable with existing instruments and/or networks, and adaptable to future ones.

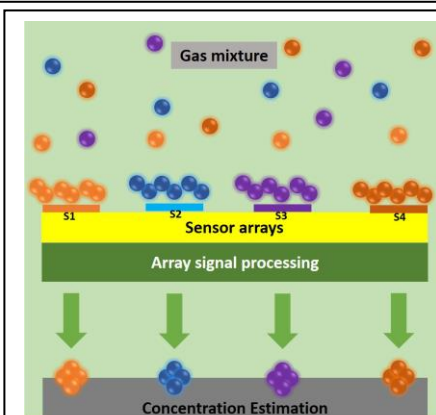
### Overall sensor system

The functional diagram of the MGSS is shown in **Figure 1a**. The MGSS will have three major components: microsensor arrays (i.e. IL electrochemical sensor and piezoelectric QTF sensor), microelectronics (i.e. potentiostat (LMP91000) and Oscillation circuit), and microcontroller and LCD display. The readout microelectronics of IL sensor is a potentiostat (LMP91000). The QTF will be driven to resonance by an oscillation circuit (SN74LVCGX04). The gas concentrations are extracted from the sensor output by a microcontroller and then displayed in percentage on the LCD screen. A buzzer or a visual alarm is also integrated for alarming if the concentration of any dangerous/harmful gas exceeds the threshold level. The voltage reference chip, power management chip, potentiostat chip, oscillation circuit, and microcontroller are all miniaturized integrated circuits. The lateral dimension of the device will be similar to or less than a credit card. We can add network components to the MGSS later. Since the sensor operation and readout do not involve either high voltages or high temperatures, our gas sensor will be intrinsically safe to operate in mines. These will allow us to achieve the characteristics described above: utility, wearability, practicality, and compatibility.



### Microsensor array sensing principles and innovations

The move toward portable sensors have already favored the development of portable and chip based microelectronics instruments that can be utilized for our sensor technology, whose volume, compact size, low cost, low power consumption and responsivity offer advantages over existing sensor technology. Thus, the more crucial need in any sensor system is the microsensor arrays. As shown in **Figure 1b**, the microsensor array consists of multiple sensor units (e.g S1-S4). Each sensor unit allows selective chemical interactions of the analyte with the sensor for its detection in a gas mixture. The array signals will be analyzed to provide each analyte concentration in percentage or ppm levels for readout. Our proof-of-concept study included both miniaturized electrochemical and piezoelectric QTF sensors designed for detection of mine gases (e.g. methane, hydrogen and oxygen). As detailed in section 5 below, we found that both sensors have many advantages for the proposed MGSS for mine safety applications. The sensor array chip design allows ease of coating with sensing materials (e.g. Ionic liquids and nanocatalysts detailed in



objective 1-2 in section 5) to enhance sensing performance at the miniaturized sensor platform as well as ease of integration with other modes of the sensing (e.g. piezoelectric). The microsensor array is also designed for ease of integration with current microelectronics for a fully integrated microsensor system.

One of the major innovations of the proposed gas sensor technology is its ability to detect multiple gas species in real time using multimodal sensing approach, in an inexpensive, wearable sensor package that requires minimal power. The sensor system will not require a unique sensor for each gas, and multiple gas sensing can be integrated into the same sensor package. The complimentary nature of electrochemical and piezoelectric sensors will significantly improve detection accuracy and reliability. Below we briefly discuss our multimodal sensing principle, which will facilitate the understanding of our detailed technical components in Section 5.

**Multimodal sensing approach:** A multimodal sensor approach uses two or more different technologies or technological modes to gather information about the analytes of choice. The five human senses are one example of a multimodal sensing system: each sense provides different information about objects in our environment. Combining the input from all five senses allows us to classify and identify those objects quickly and effectively.

In our sensor technology, we will employ several different multimodal approaches, all combined into one or more sensor arrays, to extract the maximum amount of information simultaneously from the same mixture of analytes. For example, a piezoelectric sensor (e.g. quartz tuning fork detailed in Objective 4 in section 5), which operates on a principle similar to the human ear to translate movement or mass changes into an electrical signal, will be integrated with IL-EG sensor arrays (Objective 1-3 in section 5) that operate much like the human nose.

**IL-EG sensor principles:** Electrochemical sensors have similar basic components (electrodes and electrolytes) to that of a battery. The sensor typically has two electrodes (a working electrode or WE, and a counter electrode or CE which can act as a reference and is sometimes called a reference electrode or RE) that are immersed in an electrolyte solution. Electrodes and Electrolyte solutions can take many forms, and can be tailored for the specific application the sensor is designed for. One common problem with electrochemical sensors that use aqueous or water-based electrolyte solutions is that over time the water will evaporate, rendering the sensor inoperative. At that point the sensor must either be replaced, or additional water must be added to restore the sensor's functions. A major motivation for choosing ionic liquids (ILs) as sensor electrolytes is because they do not suffer from the weaknesses that affect aqueous electrolyte sensors. For example, the high temperature stability of IL materials reduces the chance of sensor failure due to temperature-induced chemical or mechanical changes. They further allow easily reproducible thin film formation for fabrication of miniaturized electrochemical gas sensors.

ILs are effectively salts in a liquid state. They are powerful solvents, and electrically conducting fluids containing organic and/or inorganic cations and/or anions (positively or negatively charged atoms or molecules, respectively). Typically, they are **liquid** below 100°C, or even at room temperature (room temperature **ionic liquids**, RTILs). Since any salt that melts without decomposing or vaporizing can potentially form an ionic liquid, ILs offer a wide range of interesting properties, and the opportunity to fine-tune those properties through careful selection of the ions involved. By using ILs as the electrolytes, which do not evaporate at ambient conditions, the dry-out problem in those traditional electrochemical sensors is almost entirely eliminated.

Electrochemical sensors can interact with gases in either of two ways: through reactions between the gas being analyzed and the electrolyte solution in the sensor, or through reactions between the analyte gas and the sensor electrode. Sensor electrodes can take many different forms, from a bare conductor to one that has been modified with a coating, such as the nanocatalysts we discussed in Objective 2 in section 5. We can use the same material to build different sensors that respond in selective ways to different gases simply by varying the methods of fabrication and/or the additives in the coating to increase

the detection sensitivity for the desired analyte. The electrolyte can also be the active sensing material, by choosing an electrolyte that undergoes a specific reaction with the desired analyte, but not with any others.

The IL-EG sensors can also employ both an impedance mode (demonstrated in prior publications) and an amperometric mode (prior publications and current work shown in Objective 1-2 in section 5), allowing detection through different means of the same analyte (for cross-validation and increased accuracy) or for the simultaneous detection of different analytes, as needed. Impedance methods can detect analytes by measuring the change of capacitance or impedance due to gas adsorption at the electrode-electrolyte interface, whereas amperometric methods require the analyte to undergo a redox reaction. Since impedance methods do not require redox activity and are often reversible, they provide valuable alternatives for gas sensing.

**Piezoelectric sensor principle:** Our IL-EG sensors can be integrated with a piezoelectric sensor (such as a QTF or a quartz crystal microbalance) for multimodal sensing. The QTF sensor detects methane by measuring the increase of the resonant frequency of QTF since methane is lighter and less viscous than air (detailed in Objective 4, section 5). This operating principle gives QTF methane sensor excellent selectivity to heavier gases such as CO<sub>2</sub>. QTFs have small size and are commercially available with a very low cost (\$0.20/unit). In addition, the physical nature (no chemical coating used) of QTF methane sensor enables long-term continuous detection with high stability. Multimodal sensing allows us to make simultaneous, real-time determinations of different properties of the same target analyte (such as sorption, partition, redox activity and density). Having these complementary data allows the sensor to cross-validate the measurement results, further increasing its selectivity and accuracy.

Here we summarize the key performance parameters, and in [section 6.0](#) we detailed key parameters for our technical readiness for Phase II study.

### **Technical readiness**

We have two major goals in our research, one is the development of practicable gas sensors that are safe enough to use in mine environments, small enough to be not just portable but wearable, and effective enough to detect multiple species of interest reliably, accurately, and quickly demand significant additional efforts toward attaining sensor miniaturization and integration, the other is the fundamental developments involved in the technology such as multimodal sensing approaches, data analysis algorithm development for the sensor array, analytical method development for on-line calibration etc. Our Phase I work detailed in [section 5.0](#) below established the proof of concept to realize miniaturized gas sensors that can be a key component for a wearable or portable device composed of our robust, long-lasting sensor chip that can also be easily replaced. Our results, both published and on-going, have demonstrated our sensor technology possesses the following unique and desirable characteristics:

**Miniaturized sensor design and fabrication:** A continuing pursuit in gas sensor development is miniaturizing gas sensors while maintaining the high analytical performance required for continuous, real-time monitoring. Miniaturization of the sensor systems reduces cost and could enable wearable distributed sensor systems for mine gas monitoring. We have designed three types of microsensor chip: metal planar electrochemical sensor chip (IL-EG) fabricated by physical vapor deposition, nanoparticle based planar electrochemical microsensor fabricated by microprinting, and quartz tuning fork sensor using the low cost off-the-shelf components. We have 1) studied the electrode geometries for IL-EG sensors; 2) identified the parameters for IL-EG sensor structure; 3) identified IL-EG sensor array structure that simplifies sensing material immobilization and permits rapid and reliable sensor testing; and 4) proved the concept of methane sensing using off-the-shelf quartz tuning fork. Our design allows easy connection with instrument electronics for sensor testing.

**Precision/reproducibility:** The microelectrochemical design and fabrication is a significant step towards practical and reproducible microsensors, addressing the key challenges associated with these systems.

We use established fabrication methods that can easily scale up, allowing inherently low cost and furnishing more reliability for our sensor system. The design also allows direct coating or printing of sensing materials (e.g. nanoparticle electrode materials and IL electrolytes) on the microsensor chip reproducibly with no lateral expansion of the sensing films (e.g., IL) and provide reproducible wettability of the electrodes with ILs facilitating the reproducible operation of sensors even at higher temperatures and with very thin films. Therefore, the stability and response time for sensor platforms can be enhanced. Miniaturized sensor design will also facilitate integrated multimodal sensors (i.e. electrochemical, piezoelectric, quartz tuning fork) to work in parallel so as to have a comparable data and environmental compensation.

- **Sensitivity:** Both our IL-EG and tuning fork microsensors for oxygen, hydrogen and/or methane have the sensitivity and linear concentration ranges needed to meet or exceed requirements for mine gas detection. We anticipate that sensitivity can be further increased by optimizing the nanoparticle catalytic activity and surface area as well as the physiochemical properties of the ILs in Phase II study.
- **Selectivity:** Both of our sensors are inherently selective: the electrochemical sensor because of the analyte redox reaction, and the QTF because of density differences. Trace water can cause interference but our study showed, it can be mitigated by selecting ILs that can form stable trace water/IL electrolyte composition such as via hydrogen bonding or using hydrophobic membranes. Trace water can also be utilized as a reactant to increase selectivity based on its unique redox features. Our microsensor for oxygen, hydrogen and methane showed good selectivity. Phase II study with a multimodal electrochemical and piezoelectric sensor array should have an unprecedented selectivity due to the two-dimensional fingerprints of analyte characteristics obtained through multimodal sensor array (i.e. electrochemical, piezoelectric and quartz tuning fork) measurements.
- **Accurate:** Orthogonal sensing by both electrochemical and piezoelectric microsensors reduces false positives. The use of monolithic arrays of multimodal transduction mechanisms (i.e. electrochemical and piezoelectric) and dynamically discriminating functions of electro-gravimetric measurements further increase the accuracy.
- **Real time:** Both our IL-EG and piezoelectric tuning fork microsensors produce measurements in real time, allowing results to be obtained very quickly.
- **Small, Low Power and Low Cost:** Both our IL-EG and tuning fork microsensors are low cost using batch fabrication and low cost manufacturing. They are compatible with inexpensive, low power and miniaturized microelectronics instrumentations that promotes portability.
- **Fast:** One step detection and sensor miniaturization help to reduce the time to reach sensing equilibrium. Furthermore, real time sensing allows kinetic analysis that is significantly faster than equilibrium based sensing.

## 5.0 Proof of Concept Evaluation

Our proof-of-concept researches are detailed in four complete manuscripts/peer reviewed publications. Here we summarize the key results from these studies to support the readiness of our sensor technology to continue toward prototype development. Oxygen, hydrogen and methane were selected as our gaseous analytes to validate our microsensor performance due to their significant relevance to mine safety. We organize our research results into four objectives with objective 1-3 for IL-EG gas sensor and objective 4 for piezoelectric quartz tuning fork (QTF) sensor development. The discussion of each objective is divided into four sections: (1) Rationale, (2) Experimental section (i.e. full description of the test configurations and conditions), (3) Test Results, and (4) Conclusions. In the appendix section, we also briefly summarize of on-going research efforts including sensor system design and fabrication and temperature effects study. These on-going works are included in the appendix section 7.0.

## Objective 1. Miniaturized IL-EG sensor characterization and validation in the presence of water interference

*Effects of Water on Ionic liquid Electrochemical Microsensor for Oxygen Sensing, Sensors & Actuators: B. Chemical, 2019, 285, 350-357.*

### 1.1 Rationale

The major interference species in the IL based electrochemical sensor is the trace water attributed to the ambient condition. Basically, ILs are polar in which some ILs are water-miscible, while other ILs are water-immiscible. Even in the case of immiscibility, ILs are generally hygroscopic and capable of solvating water from atmospheric moisture or other accessible sources of water. In the presence of water, not only will the electric double layer structure be modified, but also the reaction pathway may be changed. Thus, the development of IL-based electrochemical sensors especially microsensor and microdevice utilizing ILs requires the study of water effects in miniaturized electrochemical sensor devices.

We design and fabricate a miniaturized planar interdigitated electrochemical sensor chip shown in **Figure 1.1** that is a representation of an electrochemical microsensor device prototype. We studied the effect of water on IL planar electrochemical microsensor in the case of sensing oxygen. We selected oxygen as our model analyte and 1-Butyl-3-methylimidazolium tetrafluoroborate (BmimBF<sub>4</sub>) as a model IL electrolyte. To mimic real world sensor environment, we prepared three types of 'wet' ILs by adding 2% (volume ratio), 4% and 6% water into the original IL (the IL directly from the vendor), which were denoted as IL+2%, IL+4%, and IL+6% H<sub>2</sub>O. The water concentrations of these samples were  $0.4 \times 10^3$  ppm,  $2.05 \times 10^4$  ppm,  $3.71 \times 10^4$  ppm and  $5.36 \times 10^4$  ppm, respectively. We investigated oxygen sensing performance of the microsensor devices by using these untreated and 'wet' ILs as electrolytes. BmimBF<sub>4</sub> is hydrophilic, and it represents the IL that can readily adsorb water. The oxygen redox reaction pathway is dependent on the amount of water in the ILs. Thus this sensor system represents the most sensitive electrochemical sensor to water interference and allowed us to validate whether ILs based electrochemical sensors can be developed for real world gas sensing applications in the mines.

### 1.2 Experimental sections

#### 1.2.1. Sensor chip design and fabrication

Planar gold electrode was selected and fabricated as our IL-EG microsensor array prototype for the miniaturized mine safety gas sensor platform. The 3-electrode configuration (one outer reference electrode, two interdigitated electrodes with reduced impedance) forms each of the sensor array unit. **Figure 1.1 (c)** illustrates the detail of the interdigitated electrodes. The electrode fingers are 15  $\mu\text{m}$  wide and the gap in between is 25  $\mu\text{m}$ . We have another two designs with different inter-finger gaps. An epoxy wall surrounded the electrodes was designed to control the thickness of the ILs.

A significant advantage of microfabrication is its batch fabrication capability. The electrodes were fabricated on a single-side polished 4" diameter 500  $\mu\text{m}$  thickness silicon wafer. After growing 0.5  $\mu\text{m}$  thickness thin film SiO<sub>2</sub> as the insulator layer, 200 nm gold layer was e-beam evaporated with 10 nm titanium as the adhesion layer. Next, photolithography method was used to pattern the metal thin film. Namely, electrodes were etched from the metal thin film using a photoresist masking layer patterned photolithographically. A 50  $\mu\text{m}$  thick epoxy wall was microfabricated to surround electrodes, using SQ50, a negative photoresist. Finally, sensor dies were separated using deep reactive ion etching or wafer dicing. **Figure 1.1a** shows a finished 4" silicon wafer with 112 sensors simultaneously fabricated, significantly reducing the unit cost. The dimension of the sensor die can be further reduced based on the sensor performance parameters, allowing more devices to be fabricated on the same wafer. As shown in **Figure 1.1d**, the miniaturized sensor chip has dimensions of 10×10×0.5 mm and was assembled into an electrochemical microsensor. The microsensor consists of working (WE<sub>1</sub> and WE<sub>2</sub>), counter (CE), and reference (RE) electrodes. A current between the working and counter electrode is generated by analyte

redox reactions at the working electrode while the opposite redox reaction may take place at the counter electrode.

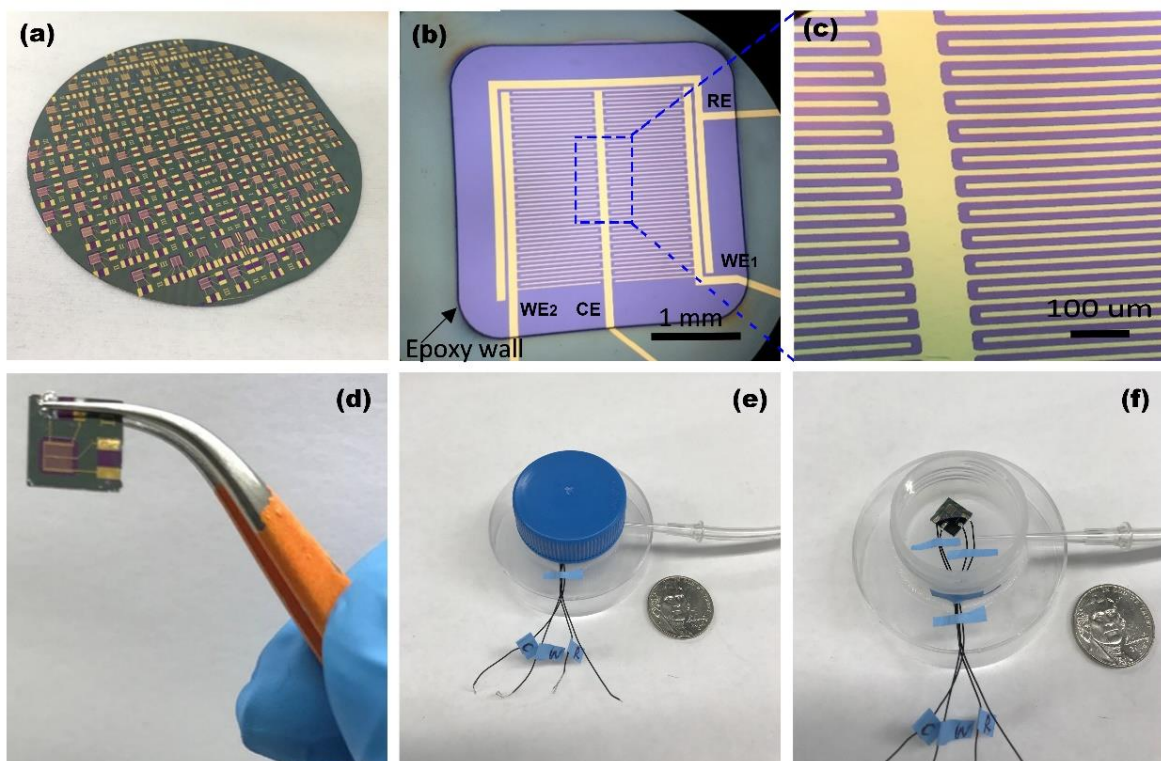


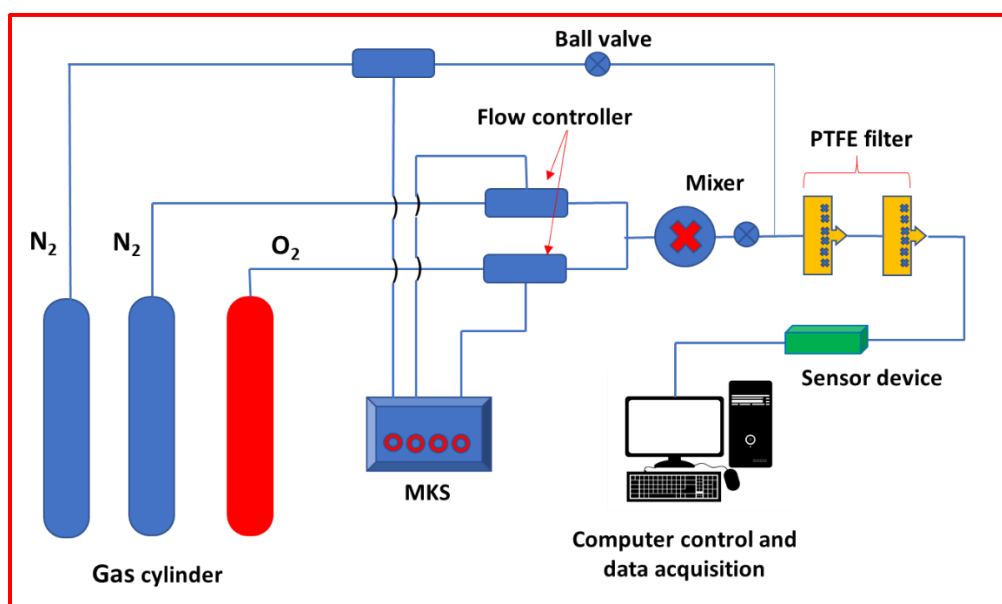
**Figure 1.1.** (a) A finished 4" silicon wafer containing 112 sensor dies. (b) Micrograph illustrating 4-electrode configuration for the gas sensor. (c) Micrograph of the interdigitated fingers. (d) The photograph of the miniaturized planar sensor chip and (e, f) home-made gas sensor testing chamber with demountable blue cap.

The microsensor device was tested as a gas sensor by incorporating it in a home-made gas sensing chamber. The working electrode ( $WE_1$ ), an auxiliary electrode or counter electrode (CE) and an on chip reference electrode (RE) were connected to the electrochemical potentiostat. Auxiliary working electrode ( $WE_2$ ) was not used in this work and will be used in Phase II multimodal sensor development. 1  $\mu$ L of IL, BmimBF<sub>4</sub>, pipetted into the sensor chip, was used for all experimental tests. All potentials were measured against an on chip gold quasi-reference electrode. All electrochemical measurements were conducted in which analyte gas and/or background gas were purged through the microsensor testing gas chamber (**Figure 1.1 e, f**). Three types of 'wet' ionic liquids were prepared by the following step: the calculated amount of BmimBF<sub>4</sub> and water (Volume ratio) were pipetted into a vial. The mixed solution was mixed at a high speed for 10 minutes on vortex mixer, and then was subsequently ultrasonically dispersed for additional 30 minutes. The obtained 'wet' ionic liquid samples were denoted as original IL (directly from the vendor), IL+2%, IL+4%, and IL+6% H<sub>2</sub>O.

### 1.2.2. Electrochemical characterization methods

All electrochemical measurements were conducted with a VersaSTAT MC potentiostat (Princeton Applied Research, USA) at room temperature. For cyclic voltammetry (CV) and electrochemical impedance spectroscopy (EIS) tests, the N<sub>2</sub> was purged into home-made gas sensor testing chamber (or O<sub>2</sub> for at least 3 h) to saturate electrolyte and then CVs were performed with 50 cycles at 100 mV s<sup>-1</sup> to

obtain a reproducible cyclic voltammogram. The CV experiments were performed between 0 to -2.0 V or 0 to -2.5 V (vs Au) in N<sub>2</sub> or O<sub>2</sub>-saturated electrolyte at 100 mV s<sup>-1</sup>. EIS experiments were carried out at a frequency range of 10<sup>-1</sup> to 10<sup>5</sup> Hz with an AC voltage amplitude of 5 mV in N<sub>2</sub> or O<sub>2</sub>-saturated IL. The chronoamperometry measurement (CA) was carried out by setting the working electrode potential at the reduction peak potential based on the CV results. Typically, the schematic illustration of the experimental setup used for CA measurement is depicted in **scheme 1.1**. The sensor chip was placed into home-made gas sensor testing chamber, where the electrochemical current of the sensor was measured as a function of time. The background gas (N<sub>2</sub> gas) was purged into the chamber for 300s. After the background current decayed to a steady value, O<sub>2</sub> gas at constant concentration was introduced into the gas chamber for 300 s and the steady state current was measured as sensing signals. All experiments were performed at room temperature (25 ± 3°C at 60 ± 5% RH) under atmospheric pressure conditions. The total gas flow rate was controlled at 50 sccm (standard cubic centimeters per minute) employing ultrapure nitrogen with controlled oxygen concentration prepared by mixing the desired gases using MKS (MKS Instruments, Inc.) type 247 4-channel readout (bundled with Mass-Flo® Controller).



**Scheme 1.1.** Schematic illustration of the experimental set-up used for gas sensing test.

### 1.3. Test Results

#### 1.3.1 Electrochemical Impedance Spectroscopy (EIS) Characterization

We carried out EIS study to characterize the impedance properties of the four types of ILs in N<sub>2</sub> and O<sub>2</sub> conditions. **Figure 1.2** depicts the Nyquist plots of EIS measurements in IL with varying amount of water. It can be seen that the serial resistance value (R<sub>s</sub>) which represents the combined contributions of ionic resistance of the electrolyte, intrinsic resistance of the substrate, and contact resistance at the active material/current collector interface, decreased gradually with increase of H<sub>2</sub>O content: 183.8Ω (IL) > 175.5Ω (IL+2% H<sub>2</sub>O) > 169.9Ω (IL+4% H<sub>2</sub>O) > 160.2Ω (IL+6% H<sub>2</sub>O), suggesting the enhanced electrical conductivity of electrolyte. The conductivity of an IL depends on the mobility of ions, which is affected by the ion size, ion association and particularly the viscosity.<sup>1-3</sup> The change in conductivity with varying water concentration in the IL can be attributed almost directly to the change of viscosity of the IL with different composition. As shown in **Figure S1.1** and **Figure S1.2** (in section 7, appendix), the contact angle measurements show that IL with the highest amount of water has the lowest contact angle on a gold substrate. This confirms higher hydrophilicity of the IL with increasing amount of water. Interestingly,

as shown in **Table S1.1**(in section 7, appendix), in all ILs studied, the  $R_s$  is higher in  $N_2$  atmosphere than that of in  $O_2$  atmosphere. The adsorption of different molecule onto the surface of electrode changes their electrical conductivity because of their different dielectric constant. Furthermore, the higher solubility of  $O_2$  in the ILs could limit the mobility of the cation and anion when  $O_2$  fills in the interspatial space of the IL. These characteristics will be studied for multimodal electrochemical sensing in Phase II work.

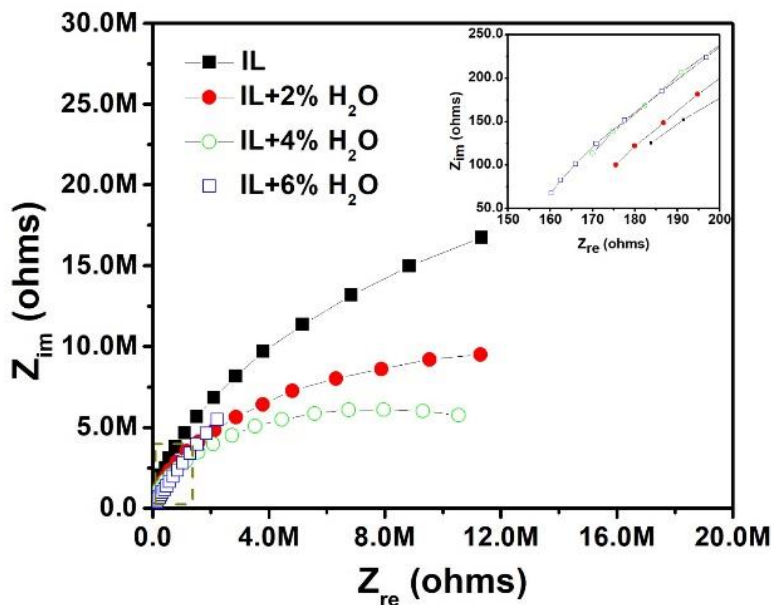
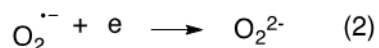
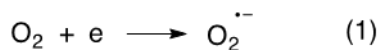


**Figure. 1.2.** EIS measurement of (a) IL (black line), (b) IL+2%  $H_2O$  (red line), (c) IL+4%  $H_2O$  (green line) and (d) IL+6%  $H_2O$  (blue line) in  $O_2$  saturated in  $BmimBF_4$ .

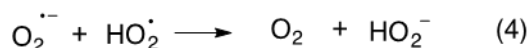
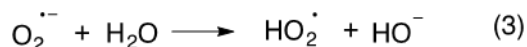
### 1.3.2. Cyclic Voltammetry Characterization

Development of an electrochemical sensor requires detailed understanding and characterization of the oxidation and/or reduction processes undergone by the analyte in the electrochemical sensor cell. Cyclic voltammetry (CV) is a very powerful tool for evaluating those redox processes. In CV, the potential is rapid sweep between two different potentials and the resulted current is measured as a function of potential. The current-potential relationship, called cyclic voltammogram, allows us to observe the behavior of a redox species of interest over a wide potential range. The CV features (shapes, number of peaks and the peak potentials) can be used to identify the gas analyte as well as for selecting the specific applied potential for the detection of the gas analyte in amperometric sensor methods.

Cyclic Voltammetry (CV) measurements were carried out in  $N_2$  or  $O_2$  saturated  $BmimBF_4$  with varying amount of water to study the effect of water on the oxygen redox processes. As shown in **Figure 1.3**, in  $N_2$  saturated original IL directly from the vendor, featureless cyclic voltammogram was observed. In contrast, when the electrolyte was saturated with  $O_2$ , the well-defined oxygen redox features appeared, which indicated the miniaturized sensor device exhibits a highly sensitive response to  $O_2$  when compared in a  $N_2$  atmosphere. Water as one of proton source plays very critical role during the electrochemical reduction of oxygen in the ILs. As shown in **Figure 1.3**, in the original IL, two well-defined redox waves were observed in the CV voltammogram with cathodic potential at -1.25 V, -1.61 V and anodic potential at -0.95 V, -1.45 V, respectively. The reduction peak potential of oxygen to superoxide in the IL with different amount of water electrolytes in **Figure 1.3** are listed **Table S1.2** (in section 7, appendix). These two stepwise reduction processes are corresponded to the following two oxygen reduction processes in the ILs<sup>4</sup>:



While reaction (1) is corresponding to  $E_{\text{Red1}}$  and reaction (2) is corresponding to  $E_{\text{Red2}}$ . In the presence of water, the  $\text{O}_2^{\bullet -}$  can react with water as described in equation (3) and (4) below to produce the hydroperoxyl radical ( $\text{HO}_2^{\bullet}$ ) and  $\text{OH}^{\bullet}$  (equation 3 and 4) <sup>5-7</sup>.



As shown in **Figure 1.4**, in the potential windows between 0 and -2.5 V, we observed an additional cathodic peak between -2.0 and -2.5V. This is due to the water reduction process ( $2\text{H}_2\text{O} + 2e \rightarrow \text{H}_2 + 2\text{OH}^-$ ) consistent with those reported in the literature<sup>8</sup>. The proton generated due to water oxidation can be reduced in the cathodic potential to form hydrogen that is shown as an anodic peak in Figure 4 between -0.5 and zero volts ( $1/2 \text{H}_2 \rightarrow \text{H}^+ + e$ ). This redox process keeps the amount of water in the IL system constant. The inset of **Figure 1.4** shows the current at an over potential of -2.5 V gradually increased with increasing of water concentration. The anodic peak current (between -0.5 and zero volts) also increases with the increasing water amount in the IL and both anodic and cathodic peak potentials shift slightly to the positive potential direction. These observations are consistent with those studies of water electrolysis in the wet IL reported in the literature<sup>8</sup>. BmimBF<sub>4</sub> is shown to be a good hydrogenation solvent and the hydrogen generated will not escape from the electrolyte interface quickly<sup>9</sup>. Furthermore, the presence of water can also change the solubility and diffusion coefficient of O<sub>2</sub> in the IL. Basically, dissolved O<sub>2</sub> gas molecule has higher diffusion coefficient and is more mobile in IL with higher amount of water than those with less amount of water, which is considered to be beneficial to charge and mass transfer <sup>10</sup>. Another significant finding is that the shape of the cathodic and anodic waves/or peaks of oxygen redox processes reflects the difference in the diffusion type of oxygen versus superoxide at the planar microsensor device. The diffusion of oxygen to the electrode is almost spherical (steady state) leading to step wise voltammetric waves whereas the diffusion of superoxide is more of planar showing a peak shaped voltammetric feature <sup>11</sup>. The linear relationship of current vs. square root of scan rate, it is concluded that the electron transfer process at the Au electrode is diffusion controlled.

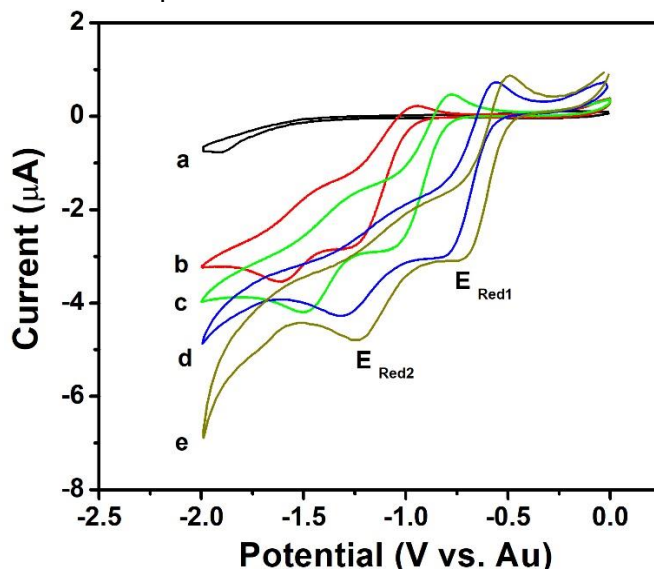


**Figure 1.3.** Cyclic voltammograms (CVs) obtained at IL-based microsensor device under (a) original IL (directly from vendor) saturated with N<sub>2</sub> gas, (b) IL (directly from vendor) saturated with O<sub>2</sub> gas, (c) IL+

2% H<sub>2</sub>O saturated with O<sub>2</sub> gas, (d) IL+ 4% H<sub>2</sub>O saturated with O<sub>2</sub> gas, (e) IL+ 6% H<sub>2</sub>O saturated with O<sub>2</sub> gas. Scan rate was 100 mV s<sup>-1</sup>.

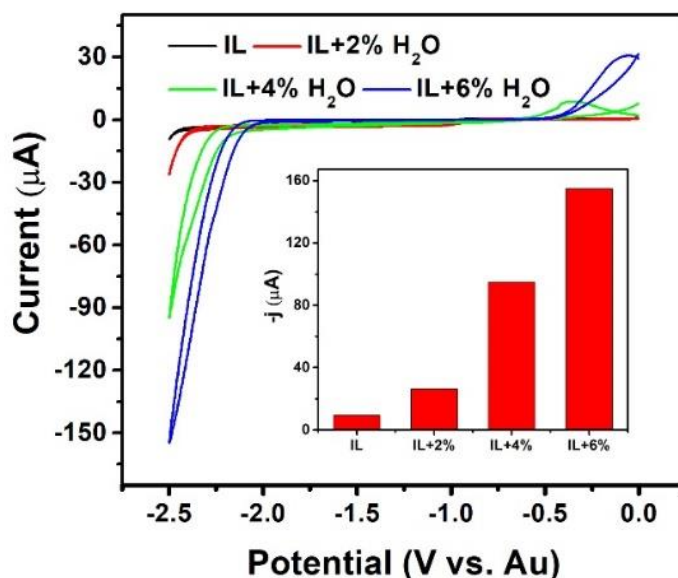


**Figure 1.4.** Cyclic voltammograms (CVs) obtained in O<sub>2</sub> saturated IL at the microsensor device under electrochemical window range from 0 to -2.5 V. Scan rate was 100 mV s<sup>-1</sup>.

### 1.3.3. Amperometric oxygen microsensor analytical performance

The constant potential chronoamperometry, also called amperometry is the simplest electrochemical technique to evaluate the performance of gas sensor. It is operated under an externally applied potential vs. reference electrode, which drives the electrode reaction of oxygen at working electrode to produce a current. This current is proportional to the oxygen concentration. The applied potential provides the selectivity for the detection. Even though ferrocene and ferrocenium (Fc/Fc<sup>+</sup>) were shown to have relative stable redox potential in the ILs and was widely used to calibrate the quasi-reference electrode potential, Fc/Fc<sup>+</sup> is not used for the potential calibration in our system since the presence of water will shift the oxygen reduction potentials. Our early work shows that oxygen reduction peak potential provides very good calibration for the redox potentials of ethyl nitrobenzene in BmimBF<sub>4</sub><sup>12</sup>. Using oxygen reduction peak to calibrate the potential shift due to the coupling reaction with water and the shift of the reference electrode potential due to the presence of water in the IL is excellent for the field application where oxygen is omnipresent. Thus, the chronoamperometry measurements were performed in which the constant potential is held at the second oxygen reduction potential in the CV experiments (i.e. -1.61 V vs Au for IL, -1.50 V vs Au for IL+2% H<sub>2</sub>O, -1.32 V vs Au for IL+4% H<sub>2</sub>O and -1.24 V vs Au for IL+6% H<sub>2</sub>O).

We thoroughly studied the sensitivity and reproducibility of the response of amperometric microsensor response using these ILs (original IL, IL+2% H<sub>2</sub>O, IL+4% H<sub>2</sub>O and IL+6% H<sub>2</sub>O) as an electrolyte under different O<sub>2</sub> concentrations. From **Figure 1.5a**, the real-time chronoamperometric signal of microsensor increases linearly with the increase of O<sub>2</sub> concentration. Notably, it exhibited good reproducibility and repeatability after 15 cycles of repeated exposure and removal of O<sub>2</sub> gas. A corresponding calibration curve of the response as a function of O<sub>2</sub> concentration was plotted. There is a good linear relationship between O<sub>2</sub> concentration and response current in all sensors (**Figure 1.5b**). Take original IL as an example, in the range of 0%-100% O<sub>2</sub>, the linear fit of corresponding response current (y) and O<sub>2</sub> concentration variation (x) is found to have a correlation coefficient of 0.9419 and a sensitivity of 0.0175 μA/%O<sub>2</sub>. This sensitivity is lower than those in the IL+2% H<sub>2</sub>O (0.0207 μA/%O<sub>2</sub>), IL+4% H<sub>2</sub>O (0.0236 μA/%O<sub>2</sub>) and IL+6% H<sub>2</sub>O (0.0252 μA/%O<sub>2</sub>). Increasing sensitivity in O<sub>2</sub> sensing is observed with higher amount of water in the ILs. Also, it is found that at the same O<sub>2</sub> concentration, for

instant, at a concentration of 20% O<sub>2</sub>, with increase of water content in the IL, the response current increases slightly: 0.8  $\mu$ A (original IL) < 0.9  $\mu$ A (IL+2% H<sub>2</sub>O) < 1.1  $\mu$ A (IL+4% H<sub>2</sub>O) < 1.4  $\mu$ A (IL+6% H<sub>2</sub>O).

In addition, the repeatability test of sensor device was performed by exposing in different O<sub>2</sub> gas concentration in IL, the period for testing time were set 10s each. The repeatability of microsensors using IL+2% H<sub>2</sub>O as electrolytes was tested because using IL+2% H<sub>2</sub>O as an electrolyte is closest to the sensor working in the real world environment and the consideration of sensing performance based on the response time and sensitivity. We repeated the experiment five times under each concentration and then used response current at 10s (the end point of sensing reaction) vs. oxygen gas concentration to plot and calculate relative standard deviation (RSD) at each concentration. As shown in **Figure 1.5c**, these curves present an increasing response current to different O<sub>2</sub> concentration, which is consistent with the chronoamperometric measurements. To characterize the repeatability of the microsensor, the largest relative standard deviation (RSD) of five repetitive tests in each oxygen concentration is calculated, which is shown in the inset of **Figure 1.5c**. From the results, the largest RSD value is 2.81% for 20% O<sub>2</sub>, which indicates the sensor exhibits good repeatability in O<sub>2</sub> sensing. Furthermore, the repeatability of microsensors using original IL and IL+2% H<sub>2</sub>O as electrolytes was assessed under the same experimental condition. The repeated tests were done five times under 20% O<sub>2</sub> concentration and the RSD of original and IL+2% H<sub>2</sub>O were calculated. These results showed that the microsensor with IL+2% H<sub>2</sub>O possessed a larger RSD value than that of original IL, which indicated the microsensor using original IL exhibited better repeatability. Additionally, we also tested the repeatability of different microsensors with IL+2% using the same testing protocol by repeating the experiment under same analyte concentration (**Figure 1.5d**) and then used response current at 10s vs. microsensor number to plot (see insert in **Figure 1.5d**). The RSD of five repetitive tests in 20% O<sub>2</sub> is 3.56%. This result suggests different sensor devices exhibited good repeatability.

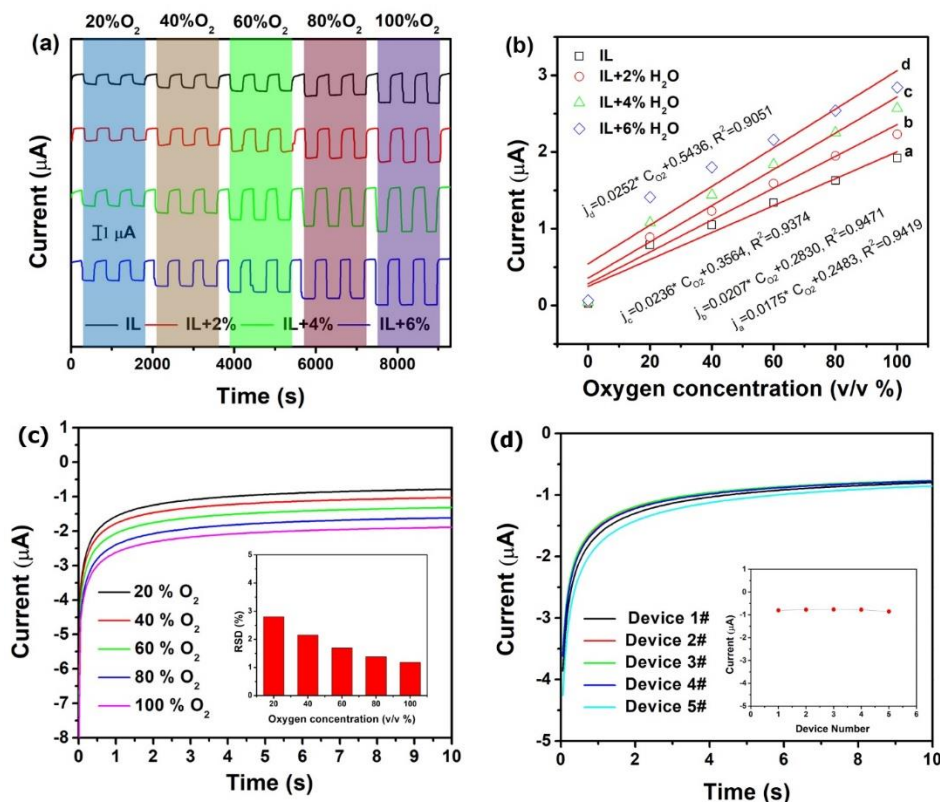


**Figure 1.5** (a) Amperometric responses of oxygen sensor; (b) The calibration curves of current. vs. oxygen concentration in original ionic liquid (black line), IL+2% H<sub>2</sub>O (red line), IL+4% H<sub>2</sub>O (green line), and IL+6% H<sub>2</sub>O (blue line). (c) The current response of the sensor for different O<sub>2</sub> concentration sensing. The inset

shows the relative standard deviation (RSD) of the single sensor device for oxygen sensing at different concentrations. Each concentration was tested for five times. (d) The current response of the sensor for 20% O<sub>2</sub> concentration sensing. The inset shows the response current at 10s of different sensors for oxygen sensing. Five sensors were tested.

### 1.3.4 Amperometric oxygen microsensor long-term stability

Water is ubiquitous in ambient mine environment. One of the major concerns for IL based electrochemical sensor is the water interference due to the varying humidity in mining conditions. The signal of electrochemical gas sensors with IL electrolytes may be affected directly by different humidity levels. Water can affect the physical and chemical properties of ILs such as viscosity, electrical conductivity as well as solvation and solubility that can further influence the sensor lifetime. The water is a proton source in the IL and the superoxide radical generated from oxygen reduction is very reactive with water. The effects of water depend on the amount of water present in the IL system, which also depends on the IL physicochemical properties. Even though ILs are non-volatile, IL can either absorb more water or the water present in the IL may evaporate. Both could change the composition of the electrolyte and consequently the signals of the IL microsenors. The BmimBF<sub>4</sub> is also shown to form hydrogen bonding with water. Thus, at a planar microelectrode microsensor, it is expected that even under gas flow conditions, water will only very slowly be lost because it is bonded with BmimBF<sub>4</sub>. Ultimately at long time, the water and BmimBF<sub>4</sub> could form a constant composition.

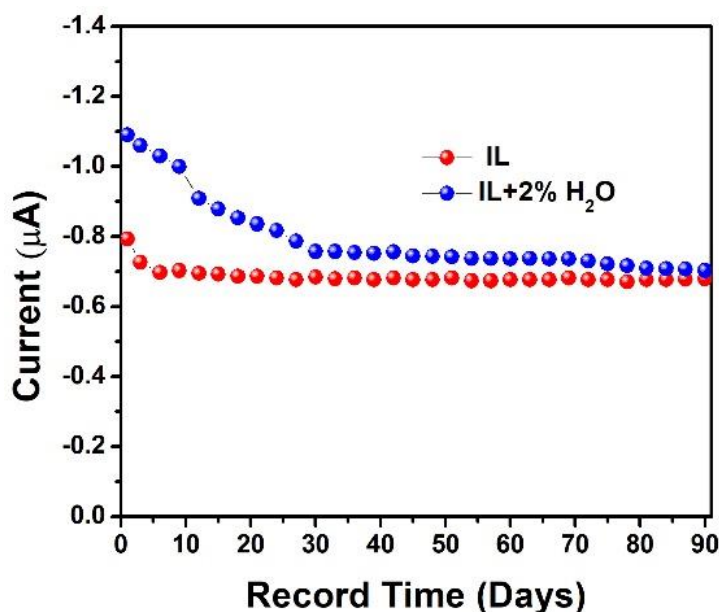


**Figure. 1.6.** Long-term stability of sensor device of IL and IL+2% H<sub>2</sub>O as an electrolyte exposed to 20% (v/v) O<sub>2</sub> in 90 days test.

We conducted a long-term stability test without maintenance of the IL based microsensor for a period of three months (**Figure 1.6**). The original IL and IL+2% H<sub>2</sub>O were used as electrolytes to assess the stability by exposing in 20% O<sub>2</sub> concentration. During this experiment, constant gas flow was maintained. The measurements were performed every 3 days for over 90 days and the sensing current was recorded. From day 1 to day 2, the change of signal in the IL is 3.8% indicating that the IL cannot be dried out easily. The observed results demonstrated that the sensing current of the sensors using original IL as an electrolyte only loss about 14.7% in 90 days, in comparison to a 35.8% loss to IL with higher amount water (IL+2% H<sub>2</sub>O). Most significantly, the IL composition will reach to a constant at extended time, the signals of original IL and IL added 2% water reach to the same current values at about 70 days. These results suggested that the sensor with original IL possess significantly better stability. After about 30 days,

the excess of water in these two ILs were lost and constant signals were obtained in both almost at the same level. As shown in the spectroscopic studies that adsorbed water in the ILs are in free state that is isolated from each other and tend to interact with the anions of the ILs forming either a 1:1 type complex,  $\text{H-O-H}\cdots\text{anion}$ , or a symmetric 1:2 type complex,  $\text{anion}\cdots\text{H-O-H}\cdots\text{anion}$  making the bonded water harder to be removed<sup>13-14</sup>. The contact angle experiments shown in **Figure S1.1** in the appendix section 7 illustrated the effects of water in the IL on the wettability of the IL/water electrolyte on gold electrode surface. The more water in the IL, the better wettability of IL on the gold electrode confirming gold electrode is hydrophilic and ionophilic. The better wettability of ILs likely slows down the drying process during experiments. Miniaturization of microsensor device with even smaller electrolyte reservoir is expected to furthermore improve the microsensor stability.

#### 1.4. Conclusions

IL based electrochemical gas sensor could experience signal drift in the real world mine condition due to the change of the sensing environments (e.g. humidity variations). The electrochemical sensing of  $\text{O}_2$  in  $\text{BmimBF}_4$  with varying water concentration in the IL electrolytes is studied using a miniaturized, planar electrochemical microsensor device. The oxygen redox processes in  $\text{BmimBF}_4$  with different amount of water were characterized systematically by cyclic voltammetry, electrochemical impedance spectroscopy and chronoamperometry using the microsensor device. The IL based microsensor's sensitivity, reproducibility, short-term and long-term stability for oxygen sensing were thoroughly characterized. Our results show that the amount of water in the IL affects the redox potential and current of the oxygen reduction signals. The redox chemistry of water in the potential window between 0 and -2.5 V kept water concentration constant. By setting the applied electrode sensing potential based on the reduction peak potential of oxygen in the CV experiment for the chronoamperometric oxygen sensor, it allows the calibration of the water coupling reaction with the oxygen reduction product and the quasi-electrode potential shifts due to the presence of water in the ILs. The good reproducibility and superior repeatability were observed for the microsensor device using IL with varying amount of water within the tested period. The microsensor using original IL directly from the vendor exhibited higher stability in comparison to those IL with added water. The stability of the oxygen microsensor is better when the water amount is smallest. In addition, the microsensor device exhibited good long-term stability when the amount of water bond with the  $\text{BmimBF}_4$  reaches a constant.

Study in Objective 1 provides the first investigation of a miniaturized planar electrochemical microsensor device employing an IL as an electrolyte with varying amount of water. Although Changes in humidity can affect signals from our IL-EG gas sensor, we are highly confident that we can address this problem. Besides the method shown in Objective 1 using oxygen reduction peak to calibrate the potential shift due to the presence of water, there are many different methods we could use to do so. For example: (i) The effect of water on the sensor operation can be compensated by integrating a humidity sensor as shown in Figure 1a, section 4.0. The specific response of the sensor with changing humidity will be determined; (ii) Thin IL films in our microsensor platform allow water concentration to be saturated quickly at various humidity levels; (iii) Our early publications showed that we can use aprotic hydrophobic ILs (e.g.  $\text{BmpyNTf}_2$ ) in which the amount of water in the ILs is very low even at high humidity to minimize the water effects; (iv) Selective gas permeable membranes can be used in sensor packaging to mitigate interference from vapors, water and other gases; (v) The presence of water may change the quasi-reference electrode potential. As detailed in objective 3 in the later section, we developed a true solid-state reference electrode that can be very valuable for addressing water effects for the stability of reference electrode in the final sensor prototype. These strategies will be studied in the Phase II work for quantitative analysis of mine gases at varying humidity levels.

## Objective 2. Miniaturized IL-EG sensor analytical performance enhancement with metal nanoparticle catalysts: design, fabrication, characterization for hydrogen and oxygen sensing

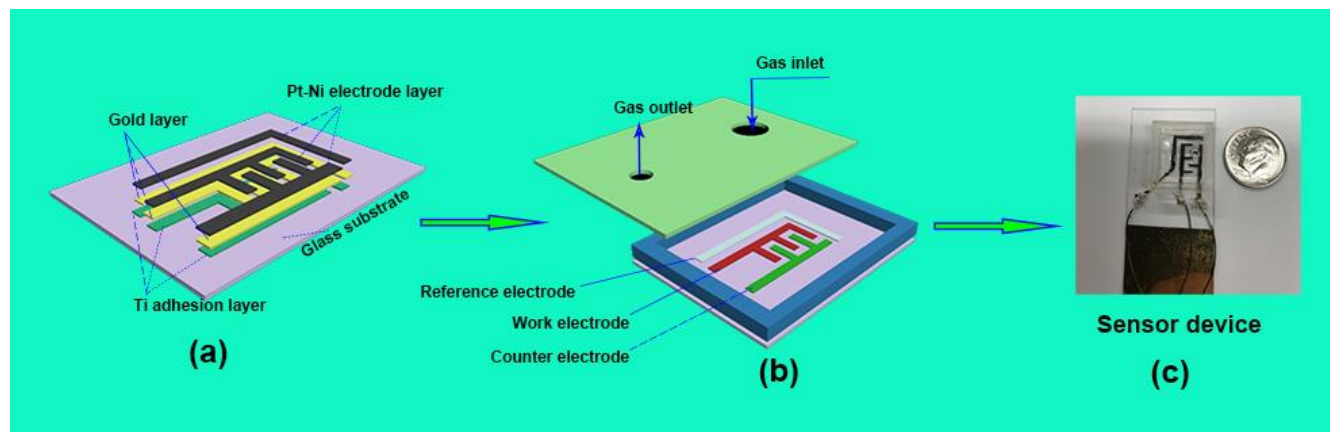
*Platinum-nickel bimetallic nanosphere and ionic liquid as sensing interface for electrochemical oxygen and hydrogen sensors, ACS Applied Nano Materials, In revision.*

### 2.1. Rationale

Miniaturization of electrochemical sensor system often requires the use of smaller sensing electrodes. Smaller electrodes result in low sensitivity since the signals of the most sensors such as electrochemical sensors are proportional to the electrode area. Nobel metal nanoparticles with controlled structures can be used as electrode materials to maximize the sensitivity and selectivity of electrochemical interface reactions based on their high surface areas and high catalytic activity. Furthermore, nanomaterials are compatible with ILs allowing stable electrolyte and electrode interface formation further increasing the sensor stability. Finally, ILs and nanomaterial are compatible with microprinting, and batch fabrication techniques for sensor miniaturization and for increasing sensor stability. Advances in nanoparticles (NP) syntheses make these materials readily available for sensor development at relatively low cost and high batch-to-batch reproducibility.

We design and synthesize a bimetallic Pt-Ni alloy NPs electrocatalyst that is expected to not only significantly reduce the cost of electrode material but also enhance the electrode activity for electrochemical sensing reactions. Pt-Ni alloy NPs were synthesized by a simple, novel solvothermal method in which dimethylformamide (DMF) and alcohol functioned as both solvent and reductant. The morphology, crystal structure and chemical composites of as-prepared Pt-Ni NPs were characterized by SEM, TEM, XRD, ICP and XPS. The Pt-Ni alloy NPs supported on carbon black (Pt-Ni/C) were used as electrode materials that were fabricated in a planar miniaturized electrochemical sensor device (**Scheme 2.1**). The wettability of the hydrophobic [Bmpy][NTf<sub>2</sub>] on the Pt-Ni/C were studied by contact angle experiments. Also, the Oxygen reduction reaction (ORR) and hydrogen oxidation reactions in [Bmpy][NTf<sub>2</sub>] at the miniaturized microsensor device were characterized by cyclic voltammetry (CV) and electrochemical impedance spectroscopy (EIS). The overall microsensor analytical properties for electrochemical sensing of gas analytes (oxygen and hydrogen) were systematically investigated by constant potential chronoamperometry.

Results show that the Pt-Ni alloys NPs not only exhibit high sensitivity, reproducibility and selectivity for sensing O<sub>2</sub> and H<sub>2</sub>, but also show good stability upon continuous use. This work demonstrates that the combination of bimetallic Pt-Ni alloys NPs as electrodes and ILs as electrolytes are promising solutions for developing highly sensitivity and selective miniaturized low-cost electrochemical gas sensors for real world sensing applications, which we will pursue in Phase II study for microsensor arrays for multiple mine gas detection.



**Scheme 2.1.** Planar microsensor device made with Pt-Ni nanocatalysts. (a) An adhesive-backed electrostatic discharge (ESD) control film (SciCron Technologies, ABF-300) was patterned by laser micromachine and attached to the Piranha cleaned glass slide as the electrode stencil, followed by 20nm Ti and 100nm Au layers deposition in an electron-beam physical vapor deposition machine (BJD 1800); then Pt-Ni NPs solution was applied through the stencil for multiple times onto the electrodes. After peeling the stencil from the glass substrate, Pt-Ni NPs coated electrodes were patterned; (b) A laser-machined acrylic case with a gas inlet and outlet was bonded onto the glass substrate for the electrochemical reaction; (c) Extension wires were connected with the 3 electrode contact pads.

## 2.2. Experimental sections

### 2.2.1. Pt-Ni alloy nanoparticle synthesis

30 mg of Pt (acac)<sub>2</sub>, 12mg of Ni(acac)<sub>2</sub>, and 50 mg of W(CO)<sub>6</sub> were subsequently added into 24 mL DMF under stirring for 20 min, afterwards, the 6mL ethanol was added to the above solution, followed by transferring the mixed solution into Teflon-lined stainless autoclave (25 mL), sealed tightly and heated from room temperature to 170 °C within 10min (the ramp is ~20 °C min<sup>-1</sup>) in a furnace. This reaction temperature was maintained for 6 h, 12 h and 24h, respectively. The stainless autoclave was then removed from the furnace and allowed to cool to ambient temperature before opening. Before washing the nanoparticles, the 60 mg of Vulcan XC 72R carbon was added into the mixing solution. The obtained mixture was ultrasonically dispersed for 30min and then stirred for several hours. Finally, the resulting product was obtained by centrifugation and completely rinsed with water and ethanol several times, followed by drying at 50 °C for 24 h. To prepare the electrode material inks, 1 mg of the as-prepared Pt-Ni/C catalyst powders was dispersed in 2 mL of 3:2 (v/v) water/ethanol mixture. After that, 40 µL Nafion solution was added into the above mixture and sonicated for 30 min to form the Pt-Ni/C catalyst ink.

### 2.2.2. Pt-Ni nanoparticle structure characterization

The morphology analysis of the obtained Pt-Ni NPs materials was carried out by a field-emission scanning electron microscopy (FE-SEM, Hitachi S-4800) and high-resolution transmission electron microscope (HRTEM, JEOL JEM-2100). X-ray diffraction (XRD) patterns were recorded at room temperature using a Bruker D8 diffractometer with Cu K $\alpha$  radiation ( $\lambda = 0.1541$  nm). The element ratio was analyzed by a Varian 725-ES inductively coupled plasma optical emission spectrometer (ICP-OES) calibrated with an in-house prepared platinum standard with a concentration of approximately 3 mg/mL. X-ray photoelectron spectroscopy (XPS) measurements were performed to examine the elemental composition and chemical state of the as-prepared sample on a PHI X-tool spectrometer with Al K $\alpha$  radiation. The contact angle measurements were carried out at room temperature on Kyowa contact angle meter (DM-CE1, Kyowa).

### 2.2.3. Planar electrochemical device fabrication procedures with Pt-Ni nanoparticles

The Pt-Ni/C catalyst ink made in 2.2.1 was used to fabricate the microsensor device on glass slides using following procedures:

1. To remove organic contaminants, glass slides (76.2 mm  $\times$  25.4 mm  $\times$  1.0 mm) were rinsed in piranha solution made of 3 parts of concentrated sulfuric acid and 1 part of 30% hydrogen peroxide.
2. Adhesive-backed electrostatic discharge (ESD) control film (SciCron Technologies, ABF-300) was patterned by laser micromachining and firmly attached to the glass slides. This film served as the lift-off stencils to pattern the electrodes. The geometric areas of working electrode (WE), counter electrode (CE) and reference electrode (RE) are around 13.5 mm<sup>2</sup>, 15mm<sup>2</sup>, and 21 mm<sup>2</sup>, respectively.
3. Electron-beam evaporation was subsequently carried out to deposit a 20 nm thick Ti adhesion layer and a 100 nm thick Au layer on the stencil-covered glass slides. This Au layer helps to reduce the electrical resistance of the NP electrodes.

4. The well-dispersed Pt-Ni catalysts ink was drop-coated by a syringe onto electrode areas opened on the stencils. The dropped ink spread on the Au surface and dried in air at room temperature. Multiple coatings were applied. The average thickness of the resulting Pt-Ni NPs layer is approximately 8  $\mu\text{m}$ .

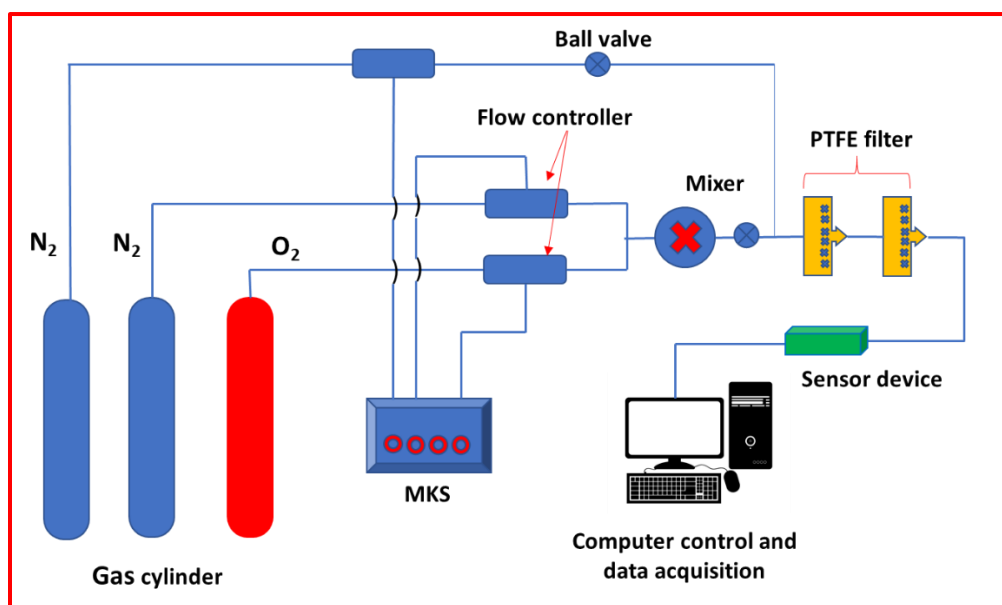
5. Then the plastic stencils were simply peeled off from the glass slides, patterning the electrodes by lifting off Au/Ti and NP layers. Unlike photolithography based lift-off process, this plastic stencil method has a high yield and avoids the use of wet solution, solvent or ultrasonic agitation, which may adversely affect the electrochemical properties of NP layer.

6. Laser-machined acrylic cases (19 mm  $\times$  17 mm  $\times$  6 mm) with gas inlets and outlets, which served as solution containers for the electrochemical reaction, were bonded on the glass slides using acrylic cement solvent.

7. Finally conductive epoxy was applied to electrically connect lead wires to the electrode pads.

#### 2.2.4. Electrochemical measurements

Electrochemical measurements were performed using a Versa STAT MC potentiostat (Princeton Applied Research, USA) with a three-electrode sensor device at room temperature. For cyclic voltammetry (CV) tests, the  $\text{N}_2$  was purged into gas sensor testing chamber (or  $\text{O}_2$  and  $\text{H}_2$  for 0.5 h) to saturate the electrolyte, and then CVs were performed with 50 cycles at  $100 \text{ mV s}^{-1}$  to obtain a reproducible cyclic voltammogram. The CV experiments were performed between 0 to -2.0 V (for  $\text{O}_2$ ) or +1.5 V (for  $\text{H}_2$ ) in  $\text{H}_2$  or  $\text{O}_2$ -saturated electrolyte at  $100 \text{ mV s}^{-1}$ . The chronoamperometry measurement (CA) was carried out by setting the working electrode potential at the reduction peak potential based on the CV results. In a typical chronoamperometry measurement shown in **Scheme 2.2**, the background gas ( $\text{N}_2$  gas) was introduced into the sensor device for 300s. After the background current decayed to a steady value, gaseous analytes ( $\text{O}_2$  or  $\text{H}_2$ ) at constant concentration was purged into the gas chamber for 300 s and the steady state current was collected as sensing signals. All experiments were performed at room temperature ( $25 \pm 3^\circ\text{C}$  at  $60 \pm 5\% \text{ RH}$ ) under atmospheric pressure conditions. The total gas flow rate was controlled at 50 sccm (standard cubic centimeters per minute) employing ultrapure nitrogen with controlled oxygen concentration prepared by mixing the desired gases using MKS (MKS Instruments, Inc.) type 247 4-channel readout (bundled with Mass-Flo® Controller).



**Scheme 2.2.** Schematic illustration of the experimental setup used for gas sensing test.

## 2.3. Test Results

### 2.3.1 Pt-Ni nanocatalyst synthesis and characterization

Surface engineering of nanomaterials plays a key role in regulating the properties and applications of electrochemical sensors.<sup>15</sup> For example, the beneficial effects due to the modified inorganics/electrolyte interfaces (e.g. adsorption of ions on inorganic surfaces, change of solvation shells of ions in the region close to inorganic surfaces, etc.) were shown to enhance ionic conductivity in the liquid.<sup>16-17</sup> The organic cation and/or anion of IL can adsorb on electrode surfaces via electrostatic interactions and orbital-overlapping interactions.<sup>18-19</sup> The ions among an IL can also interact with each other via electrostatic, hydrogen bonding and van der Waals interactions. These interactions could have several advantages in: i) improving the dispersity of nanoparticles to avoid agglomeration, ii) reducing the electrical resistance among active nanoparticles, and iii) boosting the transportation of IL electrolytes and analyte to the NPs surface. Therefore, the electrode materials are critical to tune the electrode/electrolyte interface properties towards a synergistic effect for the electrode reactions. In order to form stable IL-Pt-Ni interface, the Pt-Ni alloys catalyst should be free from the strong adsorbates during the synthesis to allow non-covalent adsorption of the ions of the IL. However, most synthetic methods for Pt nanoparticles utilize strongly adsorbing molecules (i.e. capping agents) to direct the crystal growth pathway(s) with the desired geometry. The capping agents often remain strongly adsorbed on the nanoparticle surfaces<sup>20</sup> even after the completion of the synthesis and must be removed. Complete removal of the capping agent(s) without altering the nanoparticle structure is difficult.

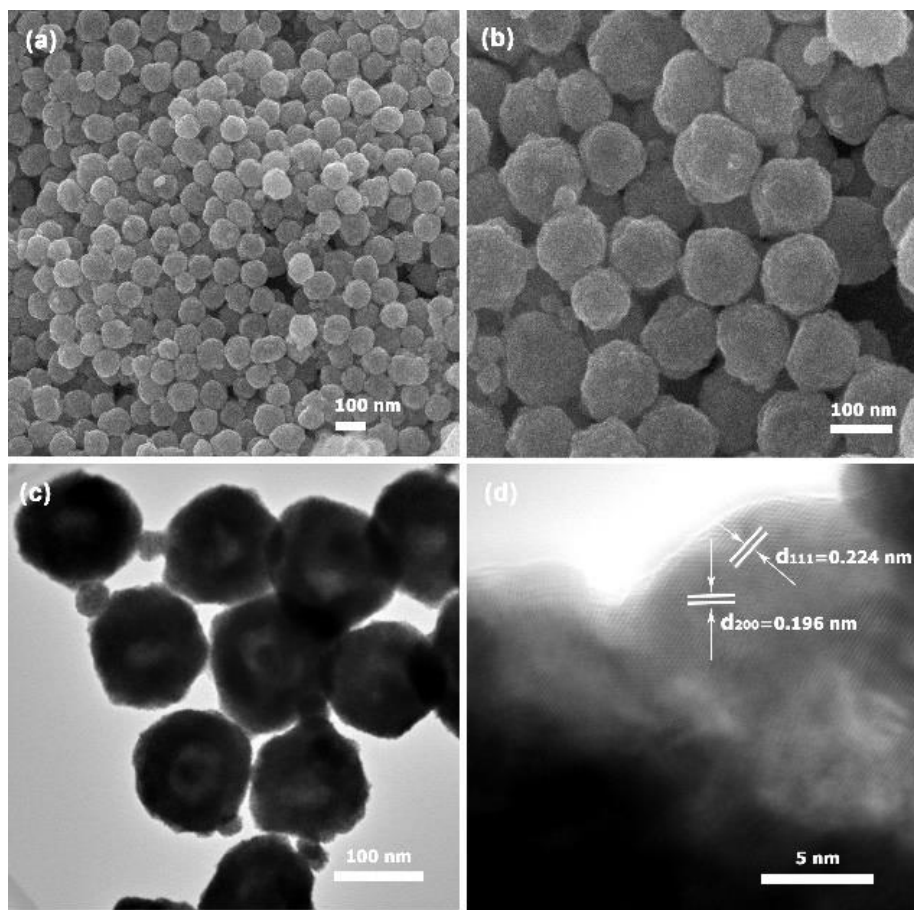


**Figure 2.1.** (a) SEM image of the Pt-Ni-12h, (b) high magnification SEM images of Pt-Ni-12h, (c) low magnification and (d) high magnification TEM image of Pt-Ni-12h.

We adapted a simple solvothermal method of synthesizing spherical Pt-Ni alloy nanoparticles without the use of capping agents reported in the literature.<sup>21-22</sup> Briefly, the spherical Pt-Ni alloy NPs were synthesized using Pt(acac)<sub>2</sub> and Ni(acac)<sub>2</sub> as metal precursors in a mixture of DMF and alcohol through simple solvothermal approach without using any bulky capping reagents. The Pt(acac)<sub>2</sub> and Ni(acac)<sub>2</sub> were mixed with W(CO)<sub>6</sub> in a mixture of DMF and alcohol. The mixture was heated to 170 °C and then maintained at this temperature for 12 h. The resulting NPs was defined as Pt-Ni-12h. When the reaction time is 6 h or 24 h, the corresponding NPs was defined as Pt-Ni-6h or Pt-Ni-24h. The morphologies of obtained Pt-Ni-12 h alloy were characterized by SEM. From the SEM images in **Figure 2.1a**, one can see that Pt-Ni-12h has spherical shape that is evenly isolated. Our study also shows that those made with 6 or 24 hours reaction time have more varied shapes and sizes. The spherical Pt-Ni particles made at 12h has a diameter of 95± 5 nm. The detailed observation at high magnification (see **Figure 2.1b**) shows the surfaces of these nanospheres are rough. The structural features of the nanospheres were further confirmed by TEM, as shown in **Figure 2.1c**. The Pt-Ni-12h particles have a relatively uniform particle size distribution and each of the nanoparticles is three dimensionally interconnected with other nanoparticles. The size of the Pt-Ni alloy nanoparticles is in the range of 90-100 nm, which is consistent to SEM observation. The crystalline structures of Pt-Ni-12 alloy nanosphere were analyzed in detail using the high-resolution TEM (**Figure 2.1d**), in which the 0.196 nm d-spacing is assigned to the Pt (200) and 0.224 nm spacing is ascribed to the Pt (111). The high crystallinity is beneficial for the adsorption of the ions of the IL to form stable interface that is important to enhance gas sensing performances.

X-ray diffraction (XRD) measurements were used to identify the internal crystalline structures of Pt-Ni NPs. **Figure 2.2** shows the XRD pattern of prepared carbon-supported Pt-Ni NPs (Pt-Ni-12h) catalysts. The broad peak at approximately 25° (2θ) is a characteristic of the (002) diffraction of carbon support. The observable diffraction peaks located at around 40.1°, 45.1° and 68° that could be assigned to (111), (200), and (220) diffractions of a face-centered-cubic (fcc) structure.<sup>23-24</sup> In particular, the peaks attributed to (111) and (200) reflections are consistent with the nanoscale structural features observed by TEM.

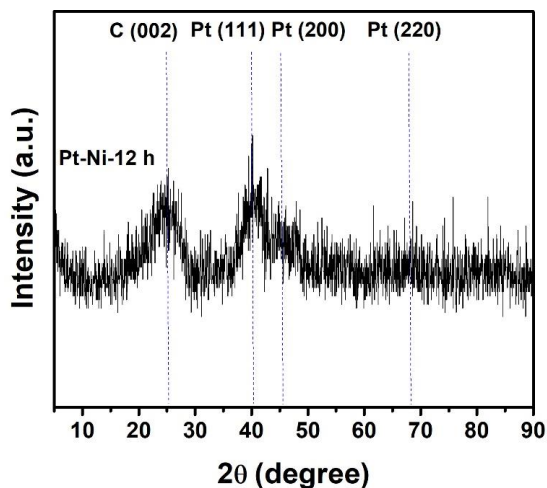


**Figure 2.2.** X-ray diffraction (XRD) patterns of Pt-Ni-12h

To explore the element properties and surface composition of the Pt-Ni/C nanomaterials, the Pt-Ni-12h nanoparticles were further analyzed by XPS. As shown in **Figure 2.3a**, the high-resolution Pt 4f spectra were deconvoluted into two doublets, with 81.2% of the Pt in the metallic state (Pt 4f) and 18.8% being oxidized (Pt<sup>2+</sup>4f). The four peaks at 71.24 eV, 74.02 eV, 74.66 eV and 77.35 eV of Pt are corresponded to the binding energy of Pt 4f<sub>7/2</sub>, Pt<sup>2+</sup>4f<sub>7/2</sub>, Pt4f<sub>5/2</sub> and Pt<sup>2+</sup>4f<sub>5/2</sub>, respectively. In **Figure 2.3b**, the high-resolution spectra of Ni 2p indicated that 64.9% of the surface Ni were in oxidized state and 35.1% were in the metallic state. Our study shows that Pt-Ni-12h exhibited the content of Ni in the metallic state (Ni 2p) is higher than that of Pt-Ni-6h with 8.5% and Pt-Ni-24h with 7.2%, which could be due to the

synthesizing time effect. As expected, the incorporation of Ni forming Pt-Ni alloy can tune the surface electronic structure of Pt metal that facilitate the oxygen reduction reaction (ORR) activity.<sup>25-27</sup> Furthermore, the tailored Pt-Ni alloy nanostructure can be impregnated with a hydrophobic IL, where the IL increases the O<sub>2</sub> solubility at the interface of Pt-Ni alloy and IL resulting in high ORR sensing activity.<sup>28-29</sup> The overall molar ratio for Pt and Ni of Pt-Ni-6h, Pt-Ni-12h and Pt-Ni-24h obtained from ICP-OES were 1:16, 1:3 and 1:3, respectively.

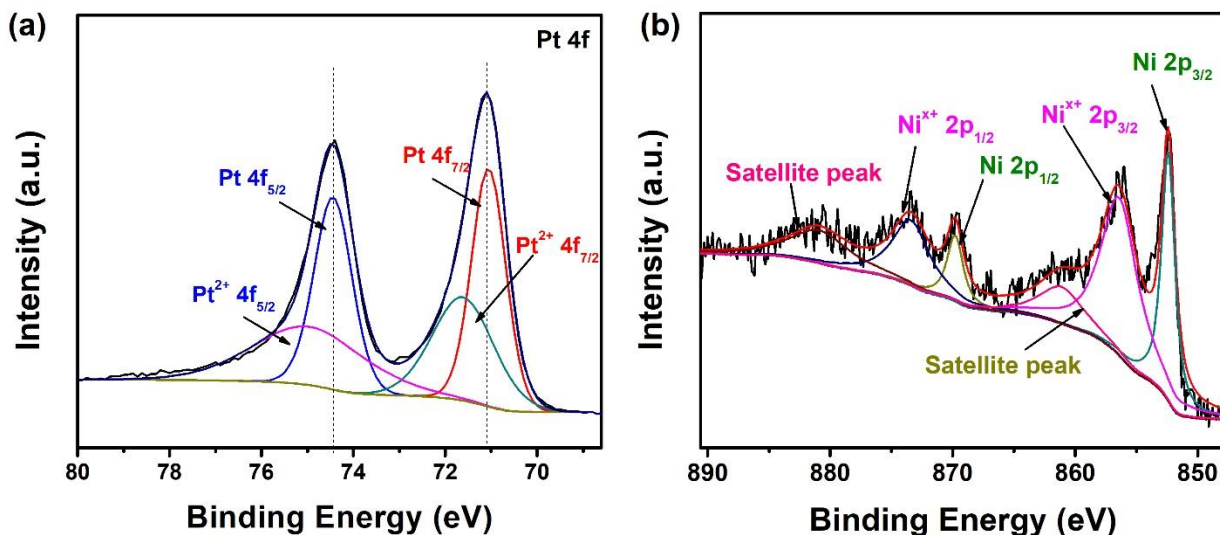


**Figure 2.3.** High-resolution XPS spectrum of (a) Pt 4f and (b) Ni 2p

### 2.3.2. Electrochemical characterizations of microsensor with Pt-Ni NP sensing materials

To validate the electrochemical properties of the Pt-Ni NPs and IL interface for electrochemical sensor application, we designed a miniaturized nanoparticle-based sensor device, consisting of a reference electrode (RE), a working electrode (WE) and a counter electrode (CE), all fabricated with Pt-Ni nanoparticles on a glass slide substrate as shown in **Scheme 2.1**. A controlled device using commercial Pt black nanoparticles (defined as Pt/C) was also fabricated and used for comparison. IL (BmpyNTf<sub>2</sub>) was selected as the electrolyte and directly added to the device. The hydrophobic BmpyNTf<sub>2</sub> was selected since contact angle experiment (discussed below) shows good wetting of it on Pt-Ni NPs. BmpyNTf<sub>2</sub> is also highly conductive with a wide stable electrochemical potential window.

We first studied the electrochemical reduction of oxygen by cyclic voltammetry (CV) using this microsensor device. The CV experiments were performed in both N<sub>2</sub> and oxygen saturated microsensor device by sweeping potential in the negative direction between 0 V and -2.0 V at a scan rate of 0.1 V s<sup>-1</sup> in. As shown in **Figure 2.4a**, the well-defined cathodic and anodic peaks appeared, which indicated the sensor device exhibits a highly sensitive response to oxygen. **Figure 2.4b** displays cyclic voltammograms of O<sub>2</sub> reduction in the microsensor device fabricated with either commercial Pt/C or Pt-Ni-12h. As expected, the improved catalytic activity of ORR reaction at Pt-Ni-12h vs. Pt/C electrode is observed. There is a significant positive potential shift of the O<sub>2</sub> reduction peak from -1.02 V for Pt/C to -0.90 V for Pt-Ni-12h, respectively. The obvious lowering of the reduction potential observed for ORR at Pt-Ni-12h is coupled to with an increased ORR current signal. This result demonstrated the superior electroactivity of Pt-Ni-12h for catalyzing oxygen reduction in O<sub>2</sub>-saturated IL. This may be attributed to several factors: first, the remarkable ORR activity is likely the result of adding Ni atoms into Pt lattice structure. Density functional theory (DFT) calculations have showed that Ni atoms in Pt lattice can modify the electronic structure of Pt due to the charge transfer from Ni to Pt, leading to a lower density of states at the Fermi level.<sup>25, 30</sup> Hence, the Pt-Ni alloys have smaller oxygen binding energies than pure Pt<sup>31</sup> which could be

beneficial to improve the ORR activity.<sup>32</sup> Second, the wettability is also a key factor to contribute the performance improvement of ORR. To measure the wetting state of the ILs on the Pt-Ni/C, the contact angle measurements were performed. For comparison, commercial Pt black (Pt/C) catalysts were measured as reference materials under the same conditions. As shown in **Table S2.1**, the contact angle of BmpyNTf<sub>2</sub> at Pt-Ni/C is 38.3 ° but on Pt/C surface is 68.2°. This suggests that BmpyNTf<sub>2</sub> wets Pt-Ni/C bimetallic nanoparticle surface much better than that on Pt/C, i.e. the adhesion of BmpyNTf<sub>2</sub> at Pt-Ni/C is better than that of Pt/C. The good wetting ability could significantly enlarge the accessible electrode surface area, enabling more effective ion transport and adsorption, which is advantageous to improve current signal and conductivity. The wettability of Pt-Ni/C in contact with commonly used hydrophilic ILs (BmimBF<sub>4</sub>) was also investigated by the contact angle measurement as a comparison. The BmpyNTf<sub>2</sub> at Pt-Ni/C exhibits better wettability than BmimBF<sub>4</sub> (see **Table S2.1**). Third, the IL-encapsulated Pt-Ni alloy structure has higher O<sub>2</sub> solubility than that of Pt/C, which is helpful to improve the ORR.<sup>28</sup> The conductivity of Pt-Ni/C and Pt/C was also compared by EIS measurement in **Figure S2.5**. The results showed Pt-Ni/C also exhibited better conductivity.

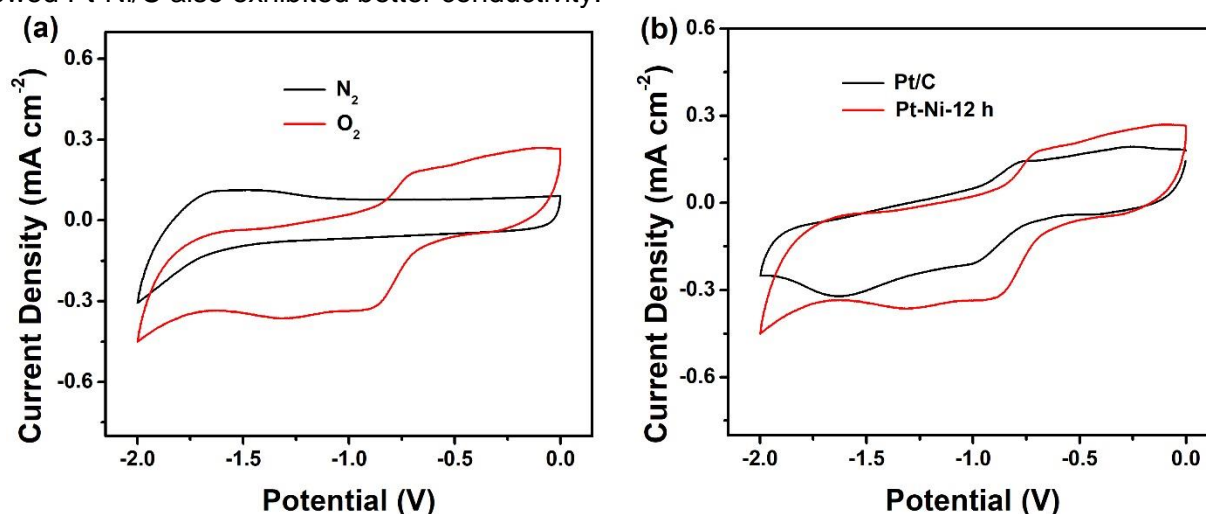


**Figure 2.4** (a) Cyclic voltammograms of Pt-Ni-12h in N<sub>2</sub> and O<sub>2</sub> -saturated ionic liquid; (b) Cyclic voltammograms of Pt/C and Pt-Ni-12 h in oxygen-saturated ionic liquid. Scan rate:100 mV s<sup>-1</sup>

### 2.3.3. Microdevice with Pt-Ni NPs and IL interface for oxygen and hydrogen sensors

The amperometric gas sensors using ILs as electrolytes were demonstrated for oxygen<sup>33-34</sup> and hydrogen sensing using home-made Clark cells in our early reports.<sup>35</sup> The spherical Pt-Ni alloy NPs combining with IL is expected to provide enhance sensitivity and stability for gas sensing in a microsensor device. The CV characterizations of ORR in the planar electrochemical microsensor device presented in **Figure 2.4** showed superior sensing activity for O<sub>2</sub> at the IL/Pt-Ni interface. Below summarized our study of constant potential chronoamperometry experiments to evaluate the analytical performance of the planar microsensor device fabricated with Pt-Ni alloys for oxygen and hydrogen gas sensing.

**Pt-Ni-IL microsensor device for oxygen sensing.** The constant potential chronoamperometry is a widely used electrochemical technique to evaluate the analytical performance of electrochemical gas sensors. The chronoamperometry measurements were performed in which the constant potential was held at the oxygen reduction potential based on the CV experiments. A potential of -1.02 V was selected for microsensor with Pt/C and -0.90 V was used for microsensor with Pt-Ni-12h. The sensitivity and reproducibility of the response of sensor device was thoroughly studied under different O<sub>2</sub> gas concentrations (v/v) from 500 ppm to 5000 ppm. As shown in **Figure 2.5a**, the real time sensing response toward different concentration of oxygen shows rapid responses that are reproducible and stable in the 15 cycles of repeated exposure and desorption of O<sub>2</sub> gas. **Figure 2.5b** shows the corresponding linear

calibration curves of the Pt/C and Pt-Ni-12h based sensor device for oxygen sensing, generated from **Figure 2.5a**, and compared with those fabricated with Pt/C. Better sensitivity (slope) is observed microsensor device fabricated with Pt-Ni-12 h in which a higher slope of  $(3.04 \pm 0.18) \times 10^{-5} \text{ mA cm}^{-2} \text{ ppm}^{-1}$  was obtained compared to that of  $(2.57 \pm 0.22) \times 10^{-5} \text{ mA cm}^{-2} \text{ ppm}^{-1}$  obtained from Pt/C based microsensor. The limit of detection (LOD,  $3s_{y/x}/b$ )<sup>36-37</sup> of Pt/C and Pt-Ni-12 h based microsensor were 218.46 ppm and 131.91 ppm, respectively, which was calculated from the calibration curves from  $s_{y/x}/b$  (where  $s_{y/x}$  is standard deviation of y- residual and b is the sensitivity).

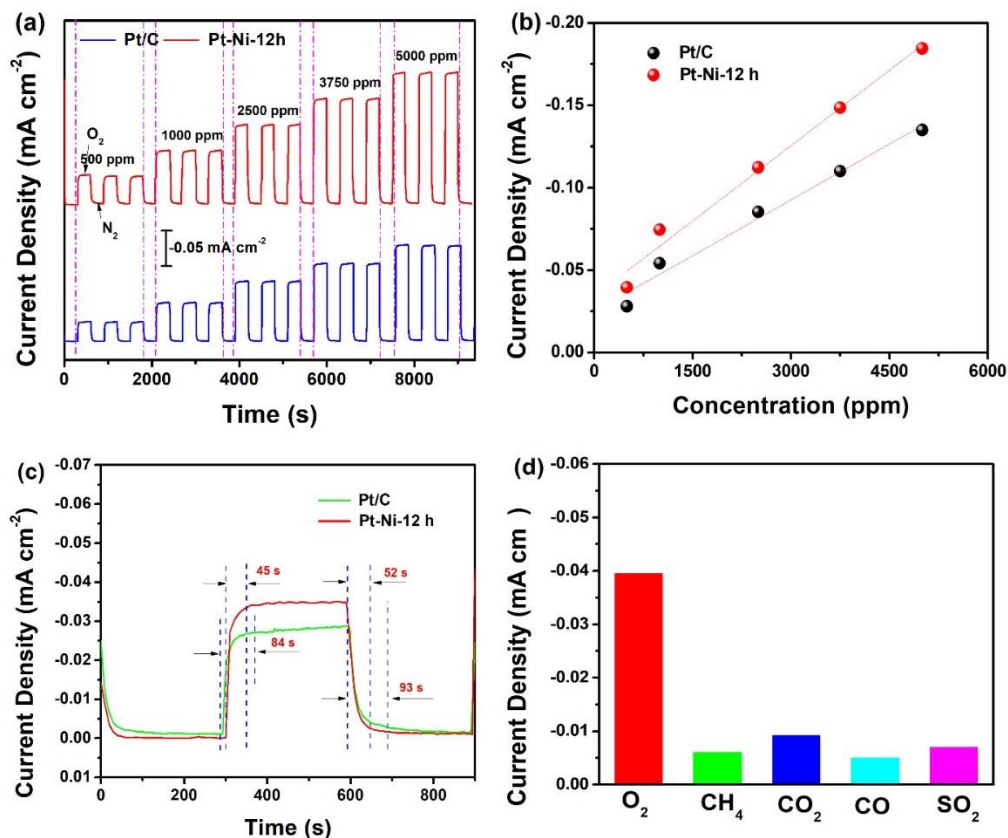


**Figure 2.5.** (a) Amperometric responses of Pt/C and Pt-Ni-12 h based microsensor toward 500 ppm to 5000 ppm O<sub>2</sub>; (b) The calibration curves of current density vs. oxygen concentration; (c) Response and recovery characteristics of the Pt/C and Pt-Ni-12 h based sensor to 500 ppm O<sub>2</sub>; (d) Selectivity of the Pt-Ni-12 h based sensor successive exposure to 5000 ppm of various gases at room temperature.

The speed of sensing response toward O<sub>2</sub> is shown in **Figure 2.5c**. The times of sensors to achieve 90% of the steady-state current density signal upon exposure to O<sub>2</sub> and N<sub>2</sub> were defined as the 90% response time ( $T_{90\text{-resp}}$ ) and the 90% recovery time ( $T_{90\text{-recov}}$ ), respectively. Note that the  $T_{90\text{-response}}$  value of Pt/C and Pt-Ni-12 h based sensor at 500 ppm are 84 s and 45 s, while the  $T_{90\text{-recovery}}$  time at 500 ppm were 93 s and 52 s, respectively. The  $T_{90\text{-response}}$  and  $T_{90\text{-recovery}}$  values of Pt-Ni-12 h based sensor was much shorter than that of Pt/C. This suggests that the primary contributions to the marked difference of the sensing activity most likely arose from the catalyst activity of Pt-Ni alloy NPs for ORR as well as superior interface properties between sensing material and IL. The response time can be further shortened with kinetics analysis methods shown in our recent work.<sup>38</sup> The kinetic analysis method can significant shorten the response time and will be further tested in our Phase II study.

Selectivity is another important factor in measuring sensor performance. Good selectivity of a target gas in the presence of various gases molecules, especially with similar chemical and physical properties,

is very important for sensors in practical applications. The selectivity of the Pt-Ni-12h based sensor has been characterized toward 5000 ppm of various interference gases including CH<sub>4</sub>, CO, CO<sub>2</sub> and SO<sub>2</sub> at operating potential of -0.90 V. As shown in **Figure 2.5d**, it is obvious that the Pt-Ni-12 h based sensor has a high response signal to 500 ppm O<sub>2</sub>, which are much higher than those to the other gases, indicating its exceptional selectivity towards O<sub>2</sub>. It is therefore safe to conclude that the Pt-Ni-12 h based sensor is a promising candidate for highly selective and sensitive detection of O<sub>2</sub>.

### ***Comparison of electrochemical sensing properties of different Pt-Ni NPs synthesized***

The unique structure features of Pt-Ni nanoparticles have important implications for their use as electrode materials to enhance the analytical performance in electrochemical gas microsensors. In order to investigate the relationship between structure and properties, the structure and sensing properties of Pt-Ni alloys NPs with different synthesized reaction time were also compared. SEM and TEM studies (**Figure 2.6**) show the morphologies of Pt-Ni NPs sample prepared at different synthesized time (6 h and 24 h). From **Figure 2.6a**, the as-obtained NP products at 6h reaction time are not uniform spherical nanoparticles, which are seriously rough and aggregated. We also characterized Pt-Ni-6h using TEM, as shown in **Figure 2.6b**. There is an obvious stack occurring, and the individual Pt-Ni nanosphere could not be clearly observed, in accordance with the SEM observations. However, when the reaction time is 12h, the well-defined uniform and monodisperse distribution with an average diameter of 100 nm nanosphere were obtained (**Figure 2.2**). From **Figure 2.6c**, with increase of reaction time up to 24 h, the surface of nanosphere seems to become rough and coalesced with the adjacent nanoparticles. The TEM observations in **Figure 2.6d**, also reveals that the nanoparticles were partly covered, which has a good agreement with the SEM image in **Figure 2.6c**.

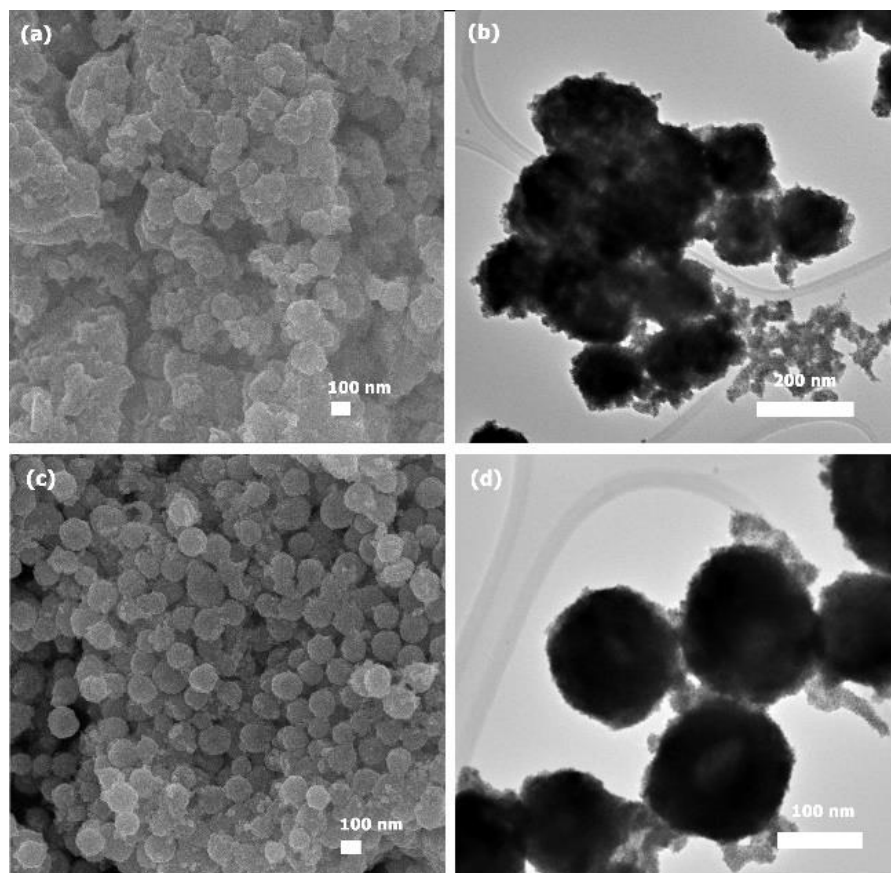


**Figure 2.6** Representative SEM and TEM images of (a, b) Pt-Ni-6h and (c, d) Pt-Ni-24 h

We have carried out electrochemical characterization of the Pt-Ni alloy NPs made at 6h, 12h and 24h in microsensor devices, the Pt-Ni-12h exhibited higher reduction current of ORR and more positive reduction potential than that of Pt-Ni-6h and Pt-Ni-24. Additionally, the EIS results displays that the Pt-Ni-12 h has better conductivity with lower serial resistance ( $R_s$ ) and charge transfer resistance compared to two other two Pt-Ni NPs samples. These differences in electrochemical properties could be related to the following factors: first, the morphology feature plays a critical role that the coalesce or aggregation of adjacent particles could lead to a decrease of electrically accessible surface area of the electrode. The cation and anion of IL couldn't adequately approach the surface of electrode and form the stable and large interface to allow efficient electronic and ionic coupling for gas sensing. Second, according to XPS analysis, the concentration of metallic state of nickel, which could greatly tune electronic structure of Pt-Ni alloys to facilitate the electrochemical activity for ORR,<sup>39-40</sup> is higher in Pt-Ni-12h than in Pt-Ni-6 and Pt-Ni-24h.

To further validate above rationalization from SEM and TEM results, the chronoamperometry measurements were also carried out to characterized real time response curves of microsensors with different Pt-Ni NPs at different  $O_2$  concentrations as displayed in **Figure 2.7a**. The results indicate that all the microsensors exhibited excellent response and recovery characteristics with respect to an  $O_2$  concentration range from 500 to 5000 ppm. A corresponding calibration curve of the response as a function of  $O_2$  concentration is plotted. From **Figure 2.7b**, it could be observed that the response increases with increasing  $O_2$  concentration from 500 to 5000 ppm for all three sensors. Among them, the response of sensor with Pt-Ni-12h to various oxygen concentrations was apparently higher than that of sensors with Pt-Ni-6 h or Pt-Ni-24h. Moreover, the response of sensor with Pt-Ni-12h did not reach saturation even at  $O_2$  concentration of 5000 ppm. This suggests that the Pt-Ni-12 h based gas sensor has a large dynamic range. Currently, we are making smaller Pt-Ni nanoparticles with new catalytic sites that should have even higher surface areas and higher surface activities to enhance microsensor analytical performance for mine gas detection (i.e. methane, hydrogen and oxygen).

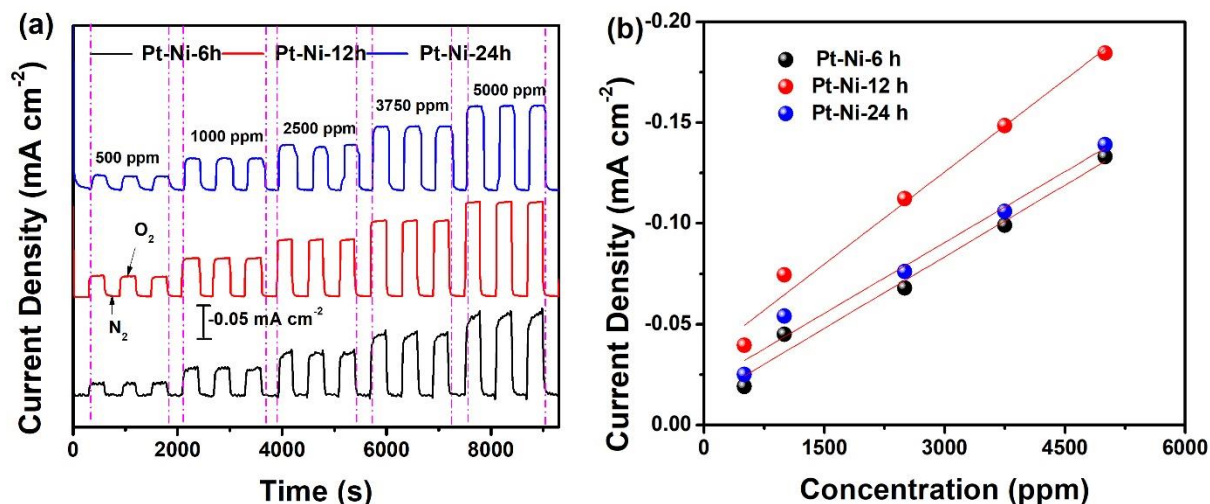


**Figure 2.7** (a) Amperometric responses of Pt-Ni-6h, Pt-Ni-12h and Pt-Ni-24h based sensor toward 500 ppm to 5000 ppm  $O_2$ ; (b) The calibration curves of current density vs. oxygen concentration.

**Pt-Ni-IL microsensor device  $H_2$  sensor.** The beneficial properties of Pt-Ni NPs and IL interface for electrochemical gas sensing of oxygen is expected to be generic. To prove this, the detailed hydrogen sensing property of the Pt-Ni alloy NPs was investigated. Hydrogen is important for mine safety applications and hydrogen oxidation reaction is possibly the most studied reaction due to its importance in fundamental and applied science.<sup>41-42</sup>

The CV and EIS results of hydrogen oxidation with these Pt-Ni alloy NPs were thoroughly characterized (data not shown). The Pt-Ni NPs shows good electrochemical activity to hydrogen oxidation. The constant potential is held at the hydrogen oxidation potential generated from CV experiment. **Figure 2.8a** shows hydrogen sensing results of microsensors made with Pt-Ni-6h, Pt-Ni-12h or Pt-Ni-24h. It can be clearly seen that three Pt-Ni microsensors showed a well-defined response when they are exposed to hydrogen gas from 500 to 6250 ppm. Additionally, it also can be observed that with increase of hydrogen concentration, the response current of three sensors gradually increased, and compared with Pt-Ni-6h and Pt-Ni-12h, the sensor with Pt-Ni-12h gave greater response current density under the same hydrogen concentration. As discussed previously, we believe this is due to forming the better reaction interface between the nanoparticles and the IL for mass and electronic transportation of gas analytes because of their differences in morphology and size of platinum-nickel alloy nanoparticles.

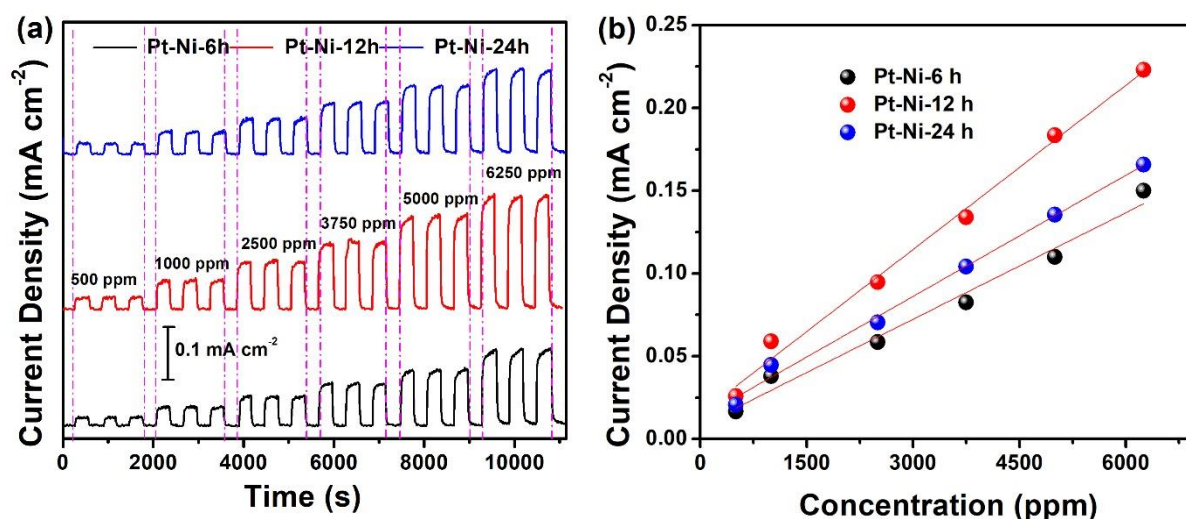


**Figure 2.8.** (a) Amperometric responses of Pt-Ni-6 h, Pt-Ni-12 h and Pt-Ni-24 h based sensor toward 500 ppm to 6250 ppm H<sub>2</sub>; (b) The calibration curves of current density vs. hydrogen concentrations.

Notably, it's worth mentioning that the microsensors with these three types of Pt-Ni NPs exhibited good reproducibility and repeatability after 18 cycles of repeated exposure and desorption of H<sub>2</sub> gas. **Figure 2.8b** shows the calibration curves of three microsensor devices with Pt-Ni NPs, generated from the data of **Figure 2.8a**. The sensitivities (slopes of calibration lines) of Pt-Ni-6h and Pt-Ni-12h, the Pt-Ni-12h were  $b = (0.215 \pm 0.014) \times 10^{-4} \text{ mA cm}^{-2} \text{ ppm}^{-1}$ ,  $b = (0.331 \pm 0.014) \times 10^{-4} \text{ mA cm}^{-2} \text{ ppm}^{-1}$  and  $b = (0.24 \pm 0.009) \times 10^{-4} \text{ mA cm}^{-2} \text{ ppm}^{-1}$ , respectively. The corresponding LOD value are 296.73, 128.40 and 142.20 ppm, respectively. In order to assess the selectivity, the selectivity of the Pt-Ni-12h based sensor has been tested toward 5000 ppm of interference gases including CH<sub>4</sub>, CO, CO<sub>2</sub> and SO<sub>2</sub> at operating potential of +0.398 V. **Figure S2.1 (in appendix Section 7.0)** shows highest selectivity of the sensor to hydrogen analyte over other interfering gases (CO<sub>2</sub>, CO, SO<sub>2</sub>, CH<sub>4</sub>).

## 2.4. Conclusions

We have synthesized Pt-Ni NPs by a simple, surfactant-free solvothermal method. The obtained Pt-Ni NPs at varying synthesis reaction times were thoroughly characterized by TEM, SEM and XPS. Contact angle experiments showed desired wettability of the IL electrolyte on the Pt-Ni nanomaterial suggesting Pt-Ni alloy NPs have balanced hydrophobic/hydrophilic properties. Planar electrochemical microsensor devices with these Pt-Ni NPs and IL BmpyNTf<sub>2</sub> were fabricated and their electrochemical properties for oxygen and hydrogen redox reactions were examined by CV and EIS. Pt-Ni NPs showed low solution and charge transfer resistance and exhibited better catalytic activity than commercial Pt black as electrode materials for oxygen and hydrogen redox reactions in the IL. Constant potential

chronoamperometry was used to characterize microsensors with Pt-Ni NP and IL sensing performance. Compared to commercial Pt/C, Pt-Ni NPs microsensor device exhibited high sensitivity, reproducibility, superior repeatability and low detection limit toward O<sub>2</sub> and H<sub>2</sub>. Not only electrode interface areas were maximized by the Pt-Ni nanomaterial, electrode selectivity was also improved owing to the unique IL-bimetallic Pt-Ni nanoelectrode interface. This study serves as a proof-of-concept that synergistically combining the benefits of ILs and bimetallic nanocatalyst can create unique interface for promoting electron/ion transports to allow highly reproducible, sensitive and selective electrochemical gas sensing at IL-electrode interface. This work demonstrates that bimetallic nanomaterial as electrodes and ILs as electrolytes are compatible with low cost microfabrication processes, and they provide synergy in electrochemical microsensors with enhanced sensitivity, specificity, and stability. The integration of organic IL and the inorganic nanocatalyst such as Pt-Ni NPs into a single planar structure will be further investigated for methane sensor development in Phase II for a miniaturized electrochemical sensor array device for monitoring multiple mine gases for mine safety and health applications.

### **Objective 3. Sensor stability enhancement: an all solid state reference electrode for microsensor application**

*A redox conjugated polymer-based all-solid-state reference electrode, Polymers, 2018, 10, 1191.*

#### **3.1 Rationale**

Electrochemical gas sensor utilizing ILs as electrolytes, quasi-reference electrodes (QRE), typically just a metal wire or band (e.g. Ag or Pt) are often used. Assuming there is no change in the bulk solution, the potential of the quasi-reference electrode will maintain as a constant during the experiments. However, the actual potential of the quasi-reference electrode vs. a true reference electrode must be calibrated under the same conditions. To further increase our microsensor stability, we developed an all-solid-state conductive polymer based true reference electrode (RE), also referred to as liquid-junction free REs that combined the benefit of both redox and conjugated polymer as a solid-state RE. Conductive polymers have inherent mechanical flexibility, printability, biocompatibility, and low cost. The liquid-junction free REs are favored to realize the miniaturization of electrochemical systems, enabling their integration onto various substrates of different sizes and shapes and in some instances may be utilized in high-pressure and high-temperature conditions. Monomer of the  $\pi$ -conjugated polymer can be easily oxidized to form thin films on various substrate through monomer electrochemical polymerization, allowing ease and controlled fabrication of conductive polymer thin films on the microsensor electrode substrates.

As shown in **Figure 3.1c**, an aniline monomer **I**, functionalized with *para*-dimethoxybenzene as latent “Pro-Redox” center was designed. The two  $\pi$ -aromatic fragments were combined with a triple bond to facilitate the efficient  $\pi$ -electron communication. The aniline and quinone moiety in poly (aniline quinone) render it to have both hydrophilic and hydrophobic compatibility with both aqueous and non-aqueous solvents so that its solvation and configuration can quickly reach to a global equilibrium in both media to provide stable electrode potential. The potential applications of this novel poly (aniline quinone) as an all-solid-state RE were tested in both aqueous and non-aqueous electrolytes.

#### **3.2. Experimental section**

##### **3.2.1 Synthesis of monomer I**

The monomer **I** was synthesized using Sonogashira coupling between 3-ethynylaniline and 2-bromo-1, 4-dimethoxybenzene, two commercially-available starting materials. The procedure is as follows: after Pd(PPh<sub>3</sub>)<sub>4</sub> (148 mg, 5% eq.), CuI (49 mg, 10% eq.), 3-ethynyl aniline (300 mg, 2.6 mmol), 2-bromo-1,4-dimethoxybenzene (612 mg, 2.8 mmol) were added to 12 mL THF/NEt<sub>3</sub> (volume ratio: 3/1) under a nitrogen atmosphere, the mixture was heated to 60°C and stirred overnight. After the solvents were removed via vacuum, the residue was extracted by ethyl acetate, dried over anhydrous sodium sulfate,

concentrated and purified by silica gel chromatography (hexane/ethyl acetate = 6/1) to obtain 3-((2,5-dimethoxyphenyl)ethynyl)aniline.  $^1\text{H}$  NMR (400 MHz,  $\text{CDCl}_3$ )  $\delta$  7.12-7.08 (t,  $J$  = 16.0 Hz, 1H), 7.01-7.00 (d,  $J$  = 2.4 Hz, 1H), 6.96-6.94 (d,  $J$  = 7.6 Hz, 1H), 6.88-6.84 (m, 1H), 6.83-6.79 (m, 2H), 6.65-6.62 (d,  $J$  = 10.4 Hz, 1H), 3.85 (s, 3H), 3.76 (s, 3H), 3.66 (s, 2H);  $^{13}\text{C}$  NMR (100 MHz,  $\text{CDCl}_3$ )  $\delta$  154.7, 153.5, 146.4, 129.4, 124.3, 122.4, 118.3, 118.2, 115.9, 115.5, 113.4, 112.5, 94.6, 93.9, 56.8, 56.0.

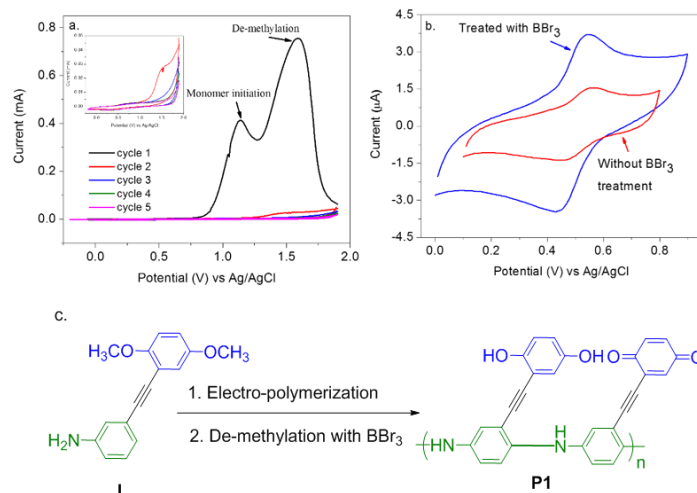


**Figure 3.1.** (a) Cyclic voltammetry of electro-polymerization of 50 mM monomer **I** in anhydrous acetonitrile with 0.1 M TBAP, potential window: -0.2 to 1.9 V, scan rate: 100 mV s<sup>-1</sup>. The inset shows cycle 2 to cycle 5. (b) Comparison of the electrochemical responses of **P1** in citric acid buffer (pH=2.0) with or without the Lewis acid (BBr<sub>3</sub>) treatment, at a sweep rate of 25 mV s<sup>-1</sup>. (c) The overall reaction scheme of electro-synthesis and de-methylation.

### 3.2.2 Electrochemical procedure

Glassy carbon working electrodes (diameter = 2 mm) were purchased from CH Instruments, Inc. and pretreated by polishing with 0.3 and 0.05  $\mu\text{m}$   $\alpha\text{-Al}_2\text{O}_3$  powder successively, followed by extensive rinsing with distilled water and ethanol and dried under nitrogen gas. The glassy carbon electrode was further conditioned by scanning between -0.5 and 1.2 V in 0.1 M  $\text{H}_2\text{SO}_4$  using cyclic voltammetry until stable current responses were obtained. During the electro-polymerization process, the glassy carbon electrode was used as the working electrode, the platinum wire (diameter = 0.5 mm) and the silver/silver chloride electrodes were used as the counter and reference electrodes respectively. The electrolytic solution consisted of 50 mM monomer in anhydrous acetonitrile with 0.1 M TBAP electrolyte. The electrochemical measurements were performed with the Gamry potentiostat, which ran the Windows XP (Gamry Instruments Inc). The electrodes were soaked in 1.0 M BBr<sub>3</sub> in dichloromethane overnight for complete removal of the methyl groups.

### 3.2.3 Electrochemical polymerization

The synthesis of polyaniline through electrochemical techniques has been established, utilizing several different approaches, ranging from potentiodynamic, potentiostatic to galvanostatic methods. Among them, the potentiodynamic technique allows the *in-situ* observance of the polymerization process<sup>25, 26</sup> and was used here. Monomer **I** does not readily dissolve in the aqueous solution, owing to its strong hydrophobic nature, even in the presence of strong acids (HCl,  $\text{H}_2\text{SO}_4$ ,  $\text{HClO}_4$ ), which are typically added for polyaniline polymerization. Several organic solvents (acetonitrile, dichloroethane and dichloromethane) were screened in our attempt to electro-polymerize **I**. **Figure 3.1a** shows the cyclic voltammograms of this process in anhydrous acetonitrile. There was no obvious difference in the

polymerization step among these three solvents. A purple-colored film of polymer was formed on the electrode surface following the electrochemical polymerization procedure.

Two distinct oxidation peaks were identified (**Figure 3.1a**): one was associated with oxidation of the aniline monomer at approximately 1.1 V, producing the cation radical for polyaniline chain growth. The other oxidation peak of approximately 1.6 V was due to the de-methylation of the parent *para*-dimethoxybenzene in the pendant group. The partial oxidation removal of the two methyl groups at ~1.6V produced the redox-active quinone/phenol from the initial redox inactive *para*-dimethoxybenzene form. Consequently, the term latent “*Pro-Redox*” center is used for reference it in monomer **I**. This partial oxidation is beneficial as some unwanted side reactions could be avoided in synthesis, if the reactive quinone or phenol structures are directly utilized. Anhydrous acetonitrile was utilized to suppress the possible electro-dimerization of dimethoxybenzene, as observed by Buck et al.<sup>40</sup>

BBr<sub>3</sub>, a strong Lewis acid, is used in chemical synthesis to remove methyl groups from methyl aryl ethers. A complex is formed between the electron-deficient boron and electron-rich oxygen, followed by bromomethane elimination to constitute the reaction mechanism.<sup>41</sup> Thus, post-polymerization modification was performed to treat the pre-formed polymeric thin film with BBr<sub>3</sub> to remove remaining methyl groups directly on the electrode surface. This two-step approach constituted an efficient sequence for **P1** formation, whose overall reaction scheme is displayed in **Figure 3.1c**. After BBr<sub>3</sub> treatment, the electrochemical response of poly (aniline quinone) **P1** was evaluated in the citric acid solution (**Figure 3.1b**). It was clear that BBr<sub>3</sub> was beneficial to enhance **P1**'s electrochemical performance, increasing the peak current by ~140%. The **P1** was first oxidized by scanning anodically. The reversible peaks of **P1** suggested that the polymerization process led to **P1** with both phenol and quinone moiety in polyaniline at a constant concentration ratio so that it will provide a constant potential.

### 3.3. Test Results

#### 3.3.1. Electrochemical properties of poly (aniline quinone) **P1**

A redox peak pair observed for **P1**, **Figure 3.1b**, is the result of the redox conversion of hydroquinone to benzoquinone with a formal potential  $E_Q^{0'}$  of 0.49 V. The surface coverage was calculated to be  $1.9 \times 10^{-8}$  mol/cm<sup>2</sup> according to  $Q/nFA$  ( $F$  is the Faraday constant and  $A$  is the electrode area). Typically, polyaniline displayed two pairs of redox peaks, corresponding to leucoemeraldine/emeraldine and emeraldine/ pernigraniline transitions respectively. Surprisingly, poly (aniline quinone) **P1** did not show these two transitions. In other words, these characteristic polyaniline peaks have been “suppressed” or “shielded” by the quinone pendant. Only the quinone/phenol conversion peaks were identified with an anodic and cathodic peak separation of 108 mV, which suggested the redox process was a two-electron transfer process. A possible explanation was the matched energy levels between polyaniline and quinone, which showed electrochemically the quinone electron transfer on a conductive substrate.<sup>42, 43</sup> It is also likely that the protons in polyaniline itself can participate in the quinone redox conversion, being consistent with the observed electro-catalytic effects of poly (2-methylaniline) and poly (3-methylaniline).<sup>39</sup> Thus, **P1**'s reversible electron transfer redox behavior of pendant quinone/phenol group is of great advantage to provide a stable reference electrode potential at electrode/solution interface since the solvent and ion transport and the polymer reconfiguration processes are very fast. The redox reaction of **P1** can be written as follows:



$$E = E^0 - 0.0592/2 \log [HQ^-]_{\text{polymer}}/[Q]_{\text{polymer}} - 0.0592/2 \text{ pH} \quad (2)$$

The electrochemical performance of **P1** was further characterized at different scan rates (**Figure 3.2a**). It was observed that the anodic peak potential shifted slightly in the positive direction with increasing scan rates while the cathodic peak potential shifted toward the negative direction. From the relationship between peak currents and scan rates, a surface-confined redox process was concluded.

The electrochemical stability of **P1** was evaluated through multiple-cycle cyclic voltammetric testing (**Figure 3.2b**). It gave very stable responses under the testing conditions. The peak current retention was excellent, being about 95% for the continuous thirty cycles (**Figure 3.2c**), which supports its long term stability as a reference electrode in microsensor device.

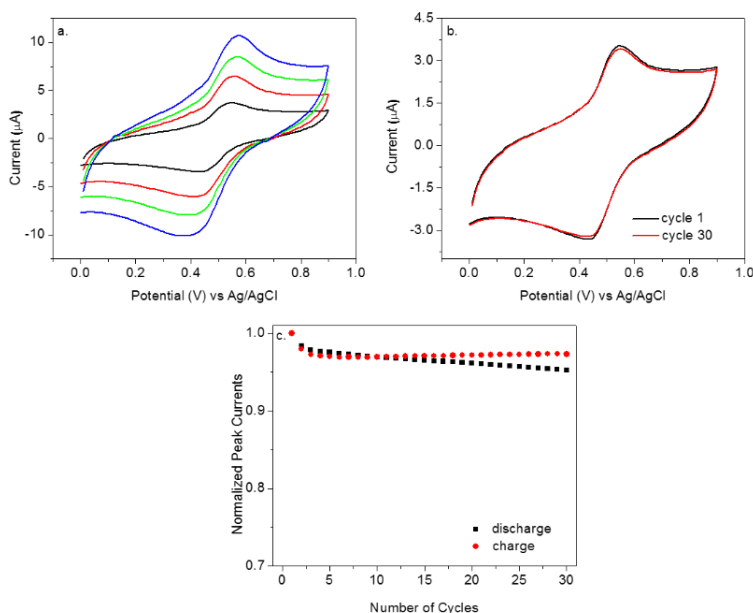


**Figure 3.2.** (a) Cyclic voltammetry of **P1** in citric acid buffer (pH=2.0) at 25, 50, 75 and 100  $\text{mV s}^{-1}$ . (b) The electrochemical cycling of **P1** in citric acid buffer (pH=2.0) at 25  $\text{mV s}^{-1}$ . (c) The normalized peak currents vs. the number of cycles.

### 3.3.2. Poly (aniline quinone) as a stable reference electrode

Unlike the aqueous systems, reference electrodes in non-aqueous solutions (organic solvents, ionic liquids and molten salts) have not been well established.<sup>14</sup> The feasibility of this novel quinone-substituted polyaniline as a RE was investigated in several non-aqueous media. Cyclic voltammetry, which features a non-zero current condition, was recorded in the presence of 1mM ferrocenemethanol (FcMeOH), using a gold electrode as the working electrode and **P1**-coated glassy carbon (GC/poly (aniline quinone)) as RE in different media. The FcMeOH redox couple exhibited typical reversible peaks and a small drift in potential was observed after 100 cycles of testing (**Figure 3.3a**), which showed the reliable stability of poly (aniline quinone) **P1** as a RE. **Figure 3.3b** compared the performance of **P1** with two other common reference electrodes of Pt and Ag/AgCl systems. The potential of **P1** RE is 0.312 V vs SCE or 0.553 V vs NHE (**Figure 3.3e**). The half-wave potential, which was the average of FcMeOH anodic/cathodic redox potentials, was monitored vs GC/**P1** RE for ten consecutive days (**Figure 3.3d**) and compared with those of Pt and Ag/AgCl as REs. A maximum drift of ~4.7 mV was observed, which showed **P1**'s excellent stability as a RE. It was kept in air without any special protection between these measurements.

### 3.3.3 Various factors to influence poly (aniline quinone) as a RE

As shown in **Figure 3.3c**, this novel polymer was compatible with various common organic solvents and [Bmim][NTf<sub>2</sub>] ionic liquid. The ferrocenemethanol (FcMeOH)'s reversible pair was used to test the RE stability. The anodic peak potentials and anodic/cathodic average of FcMeOH were similar in DCM, DCE and DMF since these solvents were polar organic solvents. The anodic peak potentials of FcMeOH in PBS, CH<sub>3</sub>CN/PBS (1:1) and CH<sub>3</sub>CN were different from these polar organic solvents as they were either aqueous or miscible with water. This finding suggested that poly (aniline quinone) showed an ideal

Nernst behavior that was solvent independent under certain conditions. This is excellent property for reference electrode in electrochemical devices. This was in great contrast to the traditional redox or conjugated polymer in which non-ideal behavior, the solvent dependence of all the equilibrium constants prevented meaningful comparison of electrochemical potential data obtained with a polymer film in different solvents.

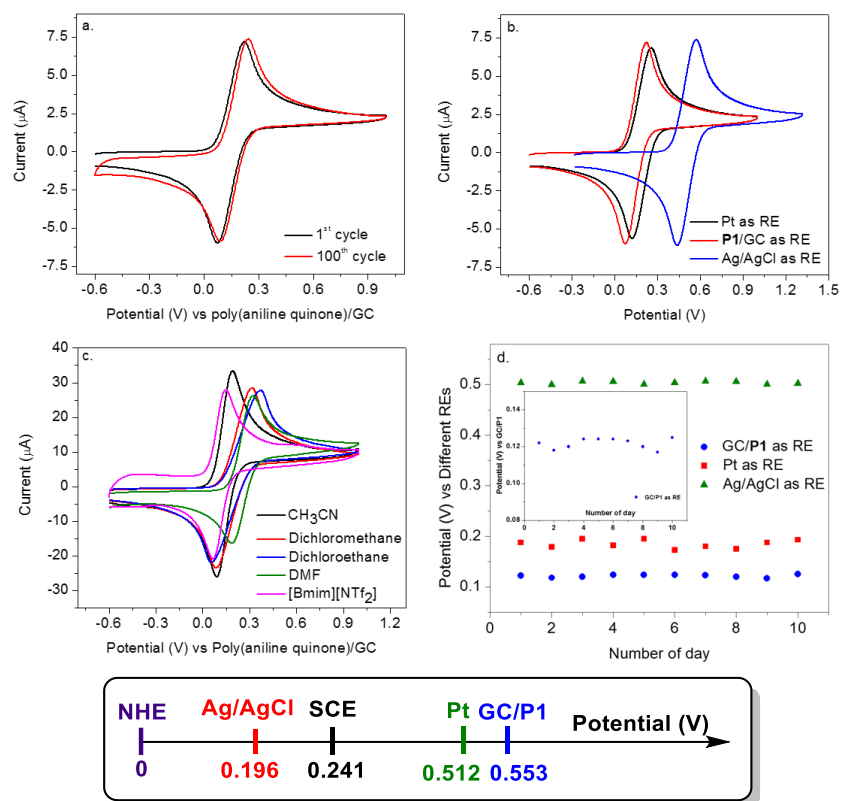


**Figure 3.3.** (a) The multi-cycle stability testing of **P1** as RE in dichloromethane solution with 0.1M TBAP electrolyte. (b) Comparison of **P1** with Pt and Ag/AgCl reference electrodes. (c) The compatibility of **P1** as RE in different non-aqueous solutions. (d) The stability of GC/**P1**, Pt and Ag/AgCl as REs in dichloromethane solution with 0.1M TBAP electrolyte. (e) Scheme displaying the potential of GC/**P1** versus the other common RE systems.

### 3.4. Conclusion

The combination of redox-active quinone and polyaniline was accomplished to give a novel redox conjugated polyaniline. The post-polymerization modification with boron tribromide furnished poly (aniline quinone) **P1** with desired properties for its use as a solid state RE. Electrochemical responses from polyaniline were “shielded” by the quinone/phenol pendants. **P1** was tested as a versatile all-solid-state plastic RE in non-aqueous and aqueous media, including various organic solvents, an ionic liquid and PBS buffer at both non-zero current and zero-current conditions. The RE was stored in the air and there were no special protection conditions needed. During ten days of continuous testing, only a small drift of ~4.7 mV in potential was observed. Thus, the unique properties of poly (aniline quinone) **P1** and its innovative polymerization methods described here show a new class of all-solid-state reference electrode that will be implemented in electrochemical microsensor devices in Phase II study.

#### Objective 4. Miniaturized quartz tuning fork sensor for methane detection

*Quartz tuning fork based methane sensor for coal mine safety application, Sensors & Actuators: B. Chemical, In revision.*

##### 4.1 Rationale

Methane sensors based on various sensing mechanisms, such as metal oxide, catalytic combustion, non-dispersive infrared (NDIR) absorption spectroscopy, have been developed. The metal oxide method is based on the conductance change of metal oxide (i.e. tin oxide) caused by the reaction with methane at elevated temperature. The catalytic combustion or pellistor methane sensor operates by combusting methane using a heated catalytic element (typically palladium). These methods are not permissible in mine environments due to high temperature used in the monitoring processes. Methane can also be detected by measuring the absorption spectrum of methane in either near infrared (IR) or mid IR bands. Mid IR method is more sensitive than near IR, but requires bulky and expensive cooling equipment for the IR sensors. We have demonstrated IL-EG methane sensors as shown in our early publications<sup>43</sup>. Our methane sensor takes the advantage of the unique coupled redox chemistry of methane and oxygen in IL [C<sub>4</sub>mpy][NTf<sub>2</sub>] at room temperature in which oxygen is first being reduced at -1.2V to superoxide and methane is being oxidized to CO and water at +0.9 V. The superoxide generated will react with CO to convert it to CO<sub>2</sub> that can further react with superoxide to generate an inert C<sub>2</sub>O<sub>6</sub><sup>2-</sup> anion as the product. Due the requirement of Pt catalysts, our IL-EG methane sensor is not as sensitive with a detection limit of 0.03%. Our on-going work is to develop new nanomaterial catalysts to further enhance our IL-EG methane sensor sensitivity and selectivity. To explore multimodal sensing for improved reliability and minimum false alarm, we developed a complementary methane sensor based on quartz tuning forks (QTFs). The operation principle is based on the fact that methane is lighter and less viscous than air and thus has less damping effect on the QTF resonator. Therefore, the presence of the methane can be detected by the increase of the resonant frequency of QTF. The advantages of QTF methane sensor include low cost (\$0.20/unit), small size, long-term continuous detection with high stability due to its physical nature (no chemical coating used), and its excellent selectivity to heavier gases such CO<sub>2</sub>.

##### Operating principle

QTFs, typically used as time-frequency standard, are commercially available with a low cost (<\$0.20/unit). QTF consists of two quartz crystal prongs that are connected at one end.<sup>44</sup> By taking advantage of the piezoelectricity of quartz, the two prongs can be actuated into out-of-phase vibration by applying an AC voltage to electrodes fabricated on the two prongs. The fundamental resonant frequency of QTF is typically 32,768 Hz in vacuum. In air, the resonant frequency drops by approximately 10 Hz. This decrease is due to the additional mass added to the vibrating prongs and the viscosity of the gas molecules. Specifically, the frequency shift can be estimated by the following equation<sup>45-46</sup>:

$$\frac{\Delta f}{f_0} = -\frac{\rho_g t}{2\rho_q w} (c_1 + c_2 \frac{\delta}{t}) \quad (1)$$

where  $\rho_g$  is the gas density,  $\rho_q$  is the effective quartz prong density including the metal electrodes,  $t$  and  $w$  are the thickness and width of the prong,  $c_1$  and  $c_2$  are geometry dependent constants.  $\delta$  is the thickness of whirl surface layer given by

$$\delta = \sqrt{\frac{\eta}{\pi\rho_g f_0}} \quad (2)$$

where  $\eta$  is the dynamic viscosity of the gas. Substituting  $\delta$  in Eq. (1) with Eq. (2), the frequency shift is

$$\frac{\Delta f}{f_0} = -\frac{t}{2\rho_q w} \left( c_1 \rho_g + \frac{c_2}{t} \sqrt{\frac{\eta\rho_g}{\pi f_0}} \right) \quad (3)$$

It can be clearly observed that the frequency shift is a function of gas density. At room temperature, the density of air is 1.225 kg/m<sup>3</sup>, whereas the density of methane is only 0.656 kg/m<sup>3</sup>. Therefore, the presence of methane will decrease the effective gas density and thus increase the resonant frequency.

It is also worth noting that the dynamic viscosities of air and methane (20 °C) are  $1.82 \times 10^{-5}$  Pa·s and  $1.10 \times 10^{-5}$  Pa·s, respectively. Therefore, the presence of methane will reduce the effective viscosity and increase the resonant frequency as well. The two terms in Eq. (3) describe the impacts of density and viscosity of ambient gas on the resonant frequency of QTF. Both mechanisms increase the resonant frequency when methane is present. Acoustic damping is neglected for QTF.<sup>46</sup>

## 4.2. Experimental Sections

### 4.2.1 Device construction

The as-received QTF (ABRACON, AB38T) is vacuum-encapsulated by a cylindrical metal case. To function as a methane sensor, the case was removed by a pair of tweezers. The two quartz prongs (5.8 mm × 1.5 mm × 0.33 mm) with electrodes can be clearly observed in **Figure 4.1 (a)**. Then the QTF was packaged inside a flow cell made of acrylic as shown in **Figure 4.1 (b)**. The plate in front of the QTF aims to avoid the direct impact of the flow on the sensor operation.

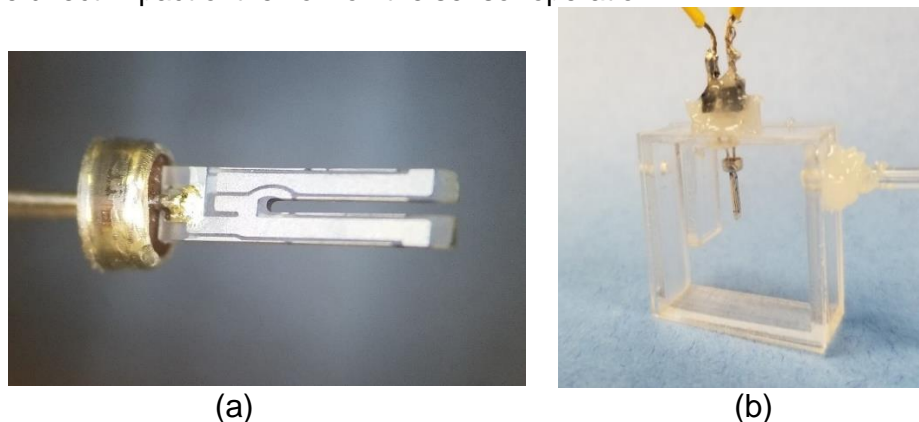


**Figure 4.1.** (a) Micrograph of a QTF (5.8 mm × 1.5 mm × 0.33 mm) with the metal case removed; (b) A QTF sensor packaged inside an acrylic flow cell.

### 4.2.2. QTF sensor testing set-up

The frequency response of the QTF in the air was characterized by sweeping the frequency of the input sinusoidal voltage generated by a function generator (Agilent 33120A) and measuring the output using a lock-in amplifier (Stanford Research SR830). Then the QTF methane sensor was characterized by injecting gases with different CH<sub>4</sub> concentrations to the acrylic cell. The CH<sub>4</sub> volume concentration  $C_{CH_4}$  was increased from 0% to 25% and then decreased to 0% with a step of 5%, while the flow rate was maintained at 100 sccm. This QTF sensor has excellent selectivity to heavier gases due to its operation principle. To verify this characteristic, the sensor's response to CO<sub>2</sub> was characterized as well. All the aforementioned tests were carried out at 23±1°C. The gas flow was controlled using MKS (MKS Instruments, Inc.) type 247 4-channel readout (bundled with Mass-Flo® Controller). Two mass-flow controllers were used to adjust the volume ratio to reach the target gas concentration. One of the mass flow controllers was used to control the background gas (Air) flow and the other was used to control the analyte gas (CH<sub>4</sub> or CO<sub>2</sub>) flow. CO<sub>2</sub> (Praxair, >99.9%) and CH<sub>4</sub> (Praxair, 99.99%) cylinder were used as the source of CH<sub>4</sub> and CO<sub>2</sub>, respectively. The gases were purged into the sensor directly. The total gas flow rate in all tests was set as 100 sccm. The resonant frequency  $f_0$  was continually recorded by a frequency counter (HP 53131A) with a sampling rate of 0.5 Hz. The data were saved in a computer via a GPIB interface. The testing setup is schematically shown in **Figure 4.2**.

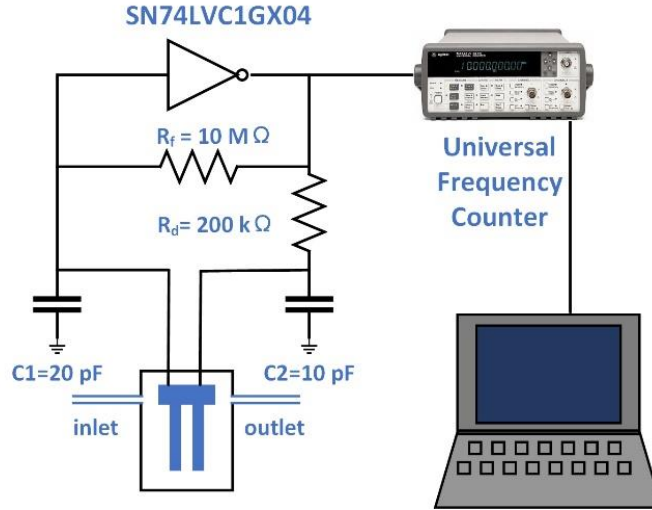


**Figure 4.2.** Schematic of the testing setup.

The temperature and pressure responses of the QTF sensor were characterized in a temperature oven (Delta Design 2300) and a vacuum chamber, respectively. The impact of humidity was studied in a sealed chamber whose humidity was varied by an ultrasonic humidifier. An Omega data logger (OM-CP-PRHTEMP101A) was used to record temperature, pressure, and humidity.

#### 4.3 Test Results

The frequency response of the QTF in the air is shown in **Figure 4.3**. The resonant frequency is 32756.3 Hz, about 11.7 Hz lower than the number in vacuum. The quality factor  $Q$  can be estimated by measuring the bandwidth over which the amplitude is  $1/\sqrt{2}$  of the resonant amplitude, i.e., full width at half maximum (FWHM). In our measurement, the FWHM is equal to  $f_+ - f_- = 32757.5\text{Hz} - 32755.1\text{Hz} = 2.4$  Hz. Therefore,  $Q$  is approximately equal to  $32756/2.4 \approx 13600$ .

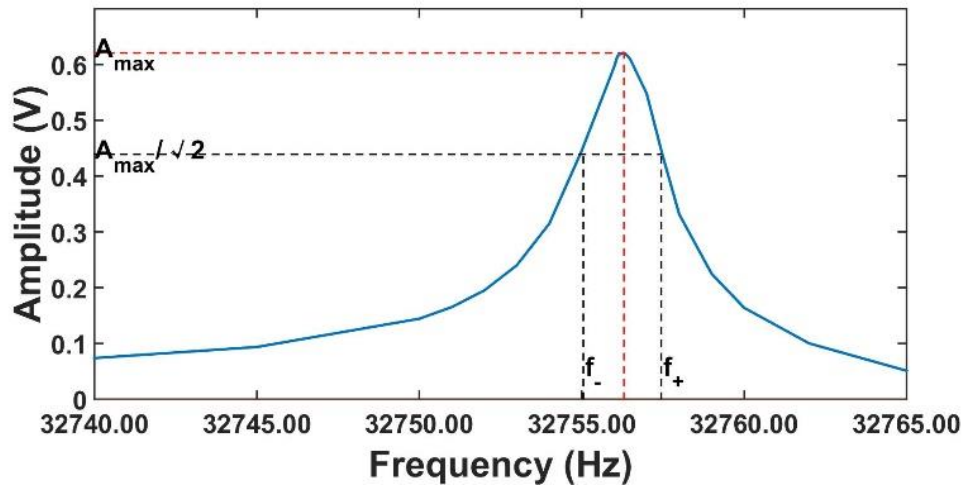


**Figure 4.3.** Frequency response of the QTF in air (23.0°C) near its resonant frequency.

**QTF methane sensor sensitivity.** The resonant frequency  $f_0$  of the QTF when the flow cell was purged with CH<sub>4</sub>/air mixtures with different CH<sub>4</sub> concentrations is plotted in **Figure 4.4**. CH<sub>4</sub> volume concentration  $C_{CH_4}$  increased and decreased for two cycles with a step size of 5%. The flow rate was maintained at 100 sccm. As expected,  $f_0$  shifted upward when  $C_{CH_4}$  increased. By processing the time series data,  $f_0$  as a function of  $C_{CH_4}$  is plotted in **Figure 4.4 (b)**. At 0%, the sensitivity to CH<sub>4</sub> concentration is 0.0063 Hz/1%. The fluctuations observed in **Figure 4.4 (a)** were mostly likely caused by the flow turbulence or imperfect flow control. **Figure 4.5** compares  $f_0$  fluctuations at 0% CH<sub>4</sub> for both 0 and 100 sccm flow rates, respectively. It can be observed that the flow has a significant impact on the sensor. This issue needs to be considered when designing the sensor package or the way of bringing in gas sample for real mine safety application. With 0% flow, the standard deviation of resonant frequency is only  $1.6 \times 10^{-4}$  Hz. Based on the sensitivity (0.0063 Hz/1%), this QTF methane sensor is able to detect 0.025% CH<sub>4</sub> in a stationary case. On the other hand, it is worth noting that for long-term monitoring, the accuracy of the sensor is determined by the drift due to temperature, pressure and humidity variation.

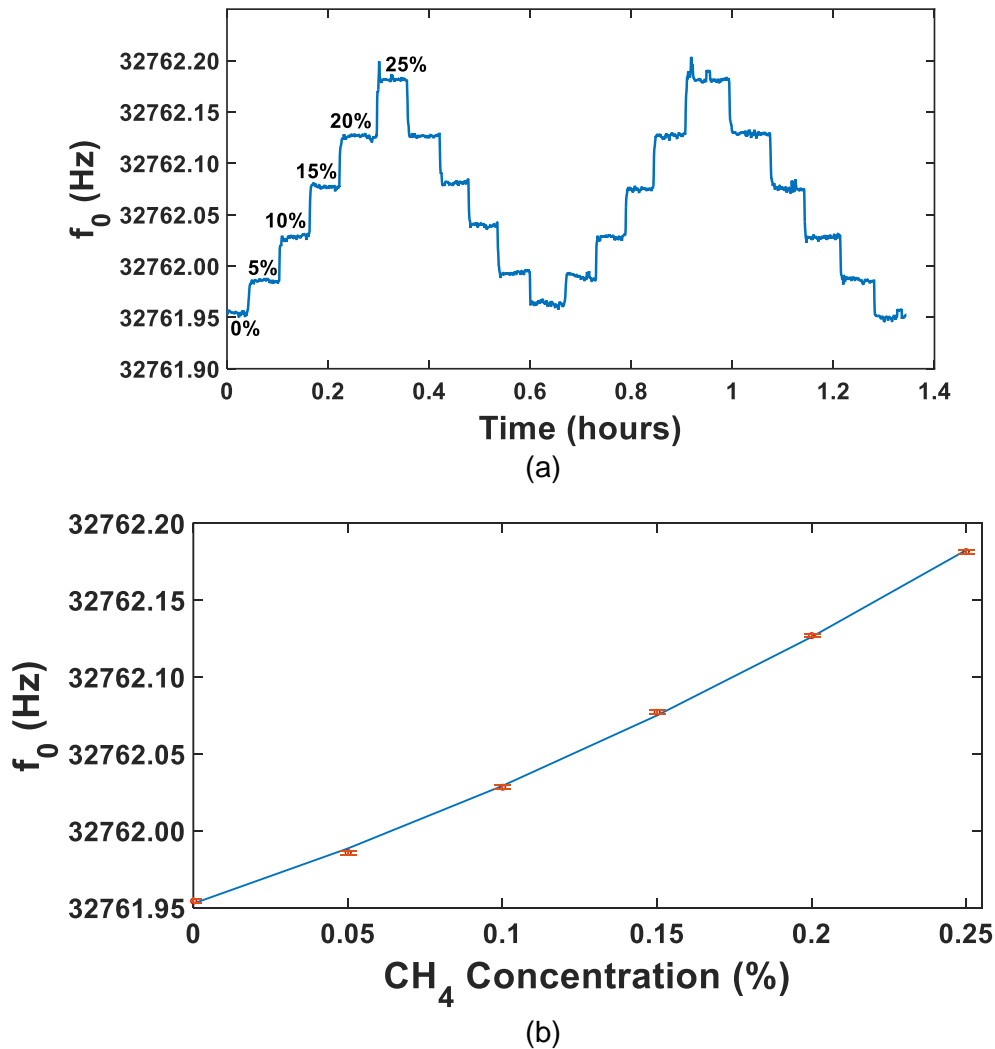


**Figure 4.4.** (a) Resonant frequency shift of the QTF as the CH<sub>4</sub> concentration varied. (b) Resonant frequency as a function of CH<sub>4</sub> concentration. The average standard deviation of the six data points is 0.0013 Hz. The test was carried out at 22.9°C.

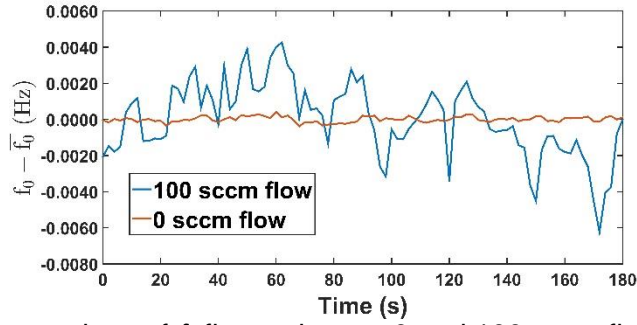


**Figure 4.5.** Comparison of  $f_0$  fluctuations at 0 and 100 sccm flow rates (0% CH<sub>4</sub>).

**QTF methane sensor selectivity.** This QTF sensor has excellent selectivity to heavier gases due to its operation principle. To verify this characteristic, we tested the sensor with CO<sub>2</sub>. **Figure 4.6** plots  $f_0$  of the QTF when CO<sub>2</sub> concentration in air was varied between 0% and 25%. As expected,  $f_0$  decreased when CO<sub>2</sub> concentration increased, opposite to CH<sub>4</sub>.

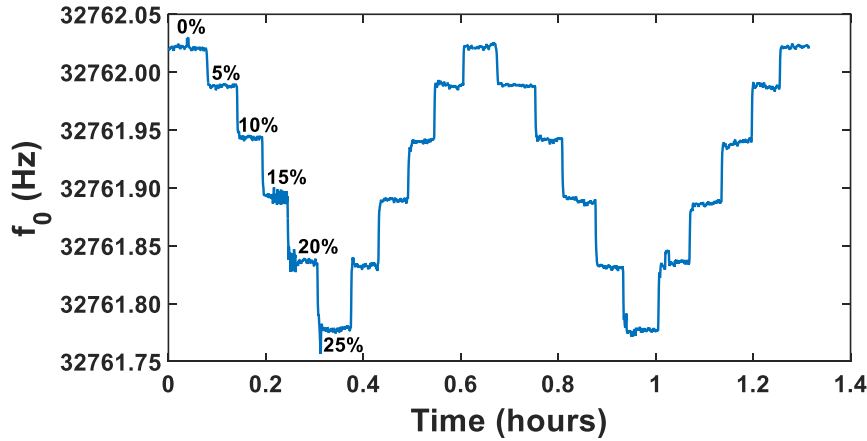


**Figure 4.6.** Resonant frequency shift of QTF as the CO<sub>2</sub> concentration (in air) varied. The test was carried out at 23.3°C.

The temperature response of QTF in ambient is illustrated in **Figure 4.7**. There are two major mechanisms that contribute to the temperature drift of QTF in air. First is the temperature response of QTF itself, i.e., due to the piezoelectric and mechanical properties of quartz. From the data sheet of ABRACON AB38T, the temperature response (in vacuum) is

$$f_0(T) = f_0(25^\circ\text{C}) \times [1 - 4 \times 10^{-8}(T - 25^\circ\text{C})^2] \quad (4)$$

In atmosphere, the temperature change leads to density and viscosity change of ambient gas, causing resonant frequency shift as well. We assume this mechanism leads to a linear shift of  $f_0$ . Therefore,  $f_0$  as a function of temperature can be fitted by the following equation:

$$f_0(T) = -0.00154(T - 25)^2 + 0.04426T + 32761.35 \quad (5)$$

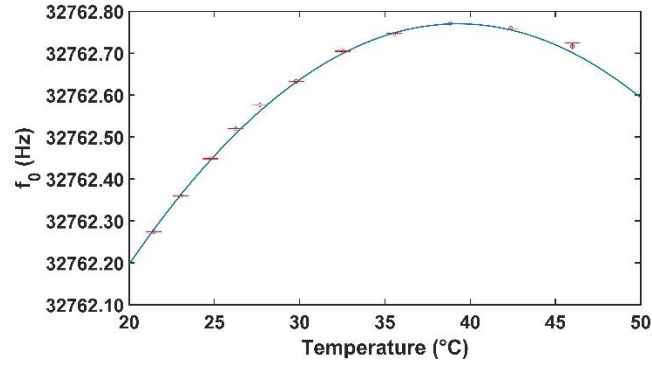


**Figure 4.7.** Temperature response of QTF sensor. The average standard deviation of data points is 0.0011 Hz.

The pressure response measurement is shown in **Figure 4.8**. A linear relationship is observed between  $f_0$  and pressure; at 23.4°C, such relationship can be described as,

$$f_0(p) = -0.005649p + 32757.76 \quad (6)$$

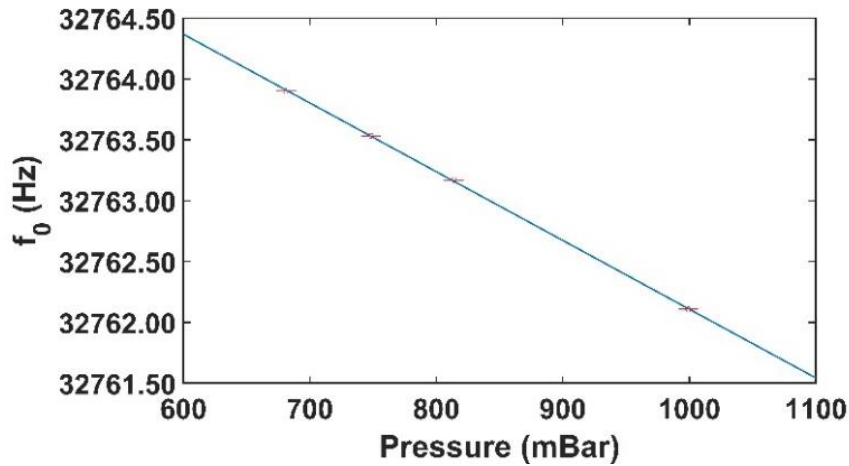


**Figure 4.8.** Pressure response of the QTF sensor at 23.4°C. The average standard deviation of data points is 0.0015 Hz.

The humidity response of QTF sensor is shown in **Figure 4.9**. After cancelling out the effects of temperature and pressure and assuming a linear model,  $f_0$  as a function of relative humidity (RH) can be described with the following equation:

$$f_0(RH) = 0.00329RH + 32759.45 \quad (7)$$

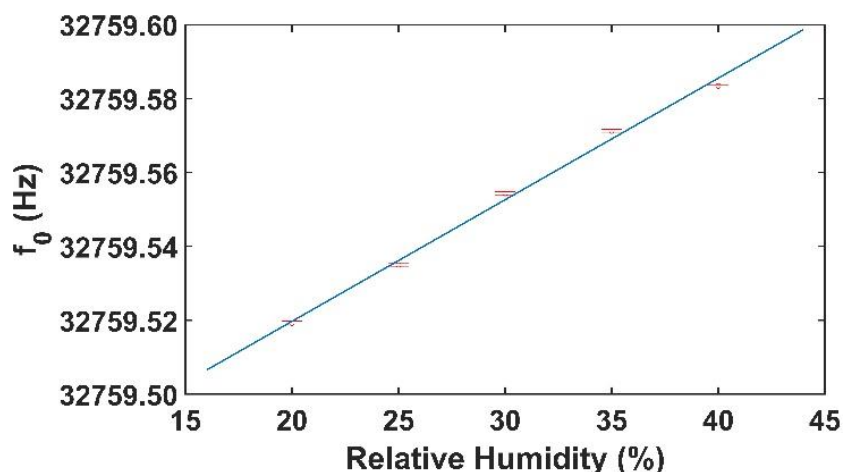


**Figure 4.9.** Resonant frequency of the QTF sensor as a function of relative humidity. The average standard deviation of data points is 0.000457Hz.

The lower and upper explosive limits of methane in air are 5% and 15-16%, respectively <sup>47</sup>. To have enough safety margin, the warning concentration of methane is often set to 0.5-1%. The detection limit or resolution of the QTF based methane sensor is 0.025%, good enough for methane monitoring in coal mines. On the other hand, it is worth noting that for long-term monitoring, the accuracy of the QTF sensor is determined by the drift due to factors such as temperature, pressure, and humidity variations. Therefore, it is necessary to integrate temperature, pressure and humidity sensors with the QTF. Moreover, the combination with other complementary methane sensors, e.g., electrochemical and quartz crystal microbalance sensors <sup>48-52</sup>, can further improve the detection accuracy and minimize false alarm.

#### 4.4 Conclusion

A methane sensor based on off-the-shelf QTFs was successfully developed. It has been demonstrated that the presence of CH<sub>4</sub> increases the resonant frequency of QTF, whereas CO<sub>2</sub> causes a decrease of the resonant frequency. The detection limit of the current QTF methane sensor is 0.025% when the sampling rate is 0.5 Hz. The impacts of temperature, pressure, and humidity have been characterized as well. The combination of QTF sensor and other complementary methane detection methods can further improve the accuracy and reliability of methane monitoring in coal mines. This will be pursued in Phase II study. Our goal is to realize a low-cost, low-power and portable methane sensor with high reliability for coal mine safety application.

#### 6.0 Technology Readiness Assessment

We have summarized the strength of our sensor design and approach in [Section 4.0](#), technical readiness part. Our research results detailed in objectives 1-4 demonstrate that the three sensor prototypes are uniquely poised to attain the concurrent goals of continuous real-time multi-gas sensing within a portable platform. Below summarize the technical milestones we accomplished in this AFC518 award that support the technology readiness of our gas sensor technology for mine safety and health application:

- A tuning fork piezoelectric methane sensor, which is robust, low cost, and low power, shows high sensitivity and selectivity for methane detection.
- Two types of planar miniaturized IL-EG sensors, one with gold metal and another with bimetallic Pt-Ni nanoparticle electrode catalysts were successfully designed and fabricated using methods that can be scaled up at low cost.

- Our testing results show both types of IL-EG sensors allow reproducible IL sensing film formation with various thicknesses as desired, increasing the accuracy of the sensor measurement.
- IL-EG sensors using nanoparticle electrode materials with controlled surface structures were shown to form better IL/electrode interfaces that were demonstrated to reduce the over potential, maximize the sensitivity and selectivity of electrochemical interface reactions.
- The miniaturized IL-EG Pt-Ni nanoparticle based sensors were tested for sensing oxygen and hydrogen gases with the sensitivity, selectivity, and stability meeting the requirement for their use in the mine conditions (see Table 1)
- Water effects on the IL-EG sensor was systematically studied using oxygen as the model analyte. Methods for calibrating water effects were established that can allow reproducible IL-EG sensor signals to be obtained. ( i.e. by using oxygen reduction peak to calibrate the potential shift due to the coupling reaction with water and the shift of the reference electrode potential due to the presence of water in the IL in field application where oxygen is omnipresent).
- An all solid conductive polymer based reference electrode was developed. It shows good potential stability in IL and traditional aqueous and non-aqueous solvents. It is excellent to be incorporated into electrochemical microsensors to further enhance the reference electrode stability.
- Temperature, humidity and pressure effects on quartz tuning fork methane sensor was characterized. The study of temperature effects on IL-EG sensors is on going.

Table 1 summarizes the key analytical parameters for the three miniaturized microsensors we developed in AFC 518 project.

<b>Table 1. Analytical specification of three types of microsensors tested in Phase I AFC 518 project</b>	
Lowest detection concentration tested	methane: 0.025% (tuning fork) hydrogen:129 ppm (Pt-Ni-12h nanoparticle IL-EG) oxygen: 132 ppm (Pt-Ni-12h nanoparticle IL-EG)
Linear range (tested)	Methane:0.025% to 5% ( tuning fork), tested for 0-25% Hydrogen: 500 to 6250 ppm ( Pt-Ni nanoparticle device) Oxygen: (i) 500ppm to 5000 ppm ( Pt-Ni nanoparticle device) (ii) 0 to 20% ( Au planar device)
Sensitivity	Methane: 0.0063 Hz/1%, (tuning fork) Hydrogen: $(0.331 \pm 0.014) \times 10^{-4} \text{ mA cm}^{-2} \text{ ppm}^{-1}$ (Pt-Ni-12h nanoparticle device) Oxygen: (1) $(3.04 \pm 0.18) \times 10^{-5} \text{ mA cm}^{-2} \text{ ppm}^{-1}$ (Pt-Ni-12h nanoparticle device) Oxygen in the presence of water: (1) 0.0175 $\mu\text{A}/\% \text{O}_2$ (original IL with less than 400 ppm water); (2) 0.0207 $\mu\text{A}/\% \text{O}_2$ (2% $\text{H}_2\text{O}$ ) (3) 0.0236 $\mu\text{A}/\% \text{O}_2$ (4% $\text{H}_2\text{O}$ ); (4) 0.0252 $\mu\text{A}/\% \text{O}_2$ (6% $\text{H}_2\text{O}$ ). Increasing sensitivity in $\text{O}_2$ sensing is observed with higher amount of water in the ILs. Also, it is found that at the same $\text{O}_2$ concentration, for instant, at a concentration of 20% $\text{O}_2$ , with increase of water content in the IL, the response current increases slightly: 0.8 $\mu\text{A}$ (original IL) < 0.9 $\mu\text{A}$ (IL+2% $\text{H}_2\text{O}$ ) < 1.1 $\mu\text{A}$ (IL+4% $\text{H}_2\text{O}$ ) < 1.4 $\mu\text{A}$ (IL+6% $\text{H}_2\text{O}$ )
Response time	Based on equilibrium (45 seconds) Based on kinetics (can be 1s or less, method was being demonstrated in early work <sup>38</sup> )
Repeatability	(i) Methane sensor: continuous sensing methane for 1.5 hours (Fig. 4.6) shows reproducible results. Output signal is frequency, which is insensitive to the voltage/power level. (ii) Pt-Ni-12h nanoparticle device tested for continuous sensing Hydrogen and oxygen over 180 hours. Reproducible results were obtained (Fig.2.7 and 2.8) (iii) Au planar device tested for oxygen sensing: relative standard deviation of five repetitive tests in 20% $\text{O}_2$ is 3.56%. 90 days test for oxygen gold planar sensor in the presence water (Fig. 1.6)
Calibration frequency	Tested, once every two month
Remote calibration	Not tested yet

Ability to measure CH <sub>4</sub> , H <sub>2</sub> , O <sub>2</sub>	Yes
Ability to measure other hydrocarbon	Feasible but not tested in this project.
Ability to isolate on site methane gas from off-site sources	Yes
Power requirements	Rechargeable battery or coin cell batteries such as Murata CR2477W (voltage: 3V; capacity: 1000 mAh, cost: \$1.20).
Power consumption	mW
Cost of sensor chip and sensing materials	~\$30 (Notes: The cost of commercially available quartz tuning forks typically ranges from \$0.10 to \$0.80, depending on the size. Our miniaturized IL-EG sensor will use very small amount of IL materials (microliter) and nanoparticle ink (microliter) that will be at a few dollars per sensor even in modest quantity. The sensor system also includes a microcontroller, a potentiostat chip, a LCD display, a battery and other components. The total cost is estimated to be around \$30)
Inherently safe	Yes
Ability to locate the emission	Possible but not tested yet
Enclosed/protected from weather	Yes
Temperature range	20 to 50 °C
Humidity	in door ( 60%) to tested for 100%
Unaffected by poisons( selectivity)	(1) CO <sub>2</sub> is not poison for methane tuning fork sensor; (2) CH <sub>4</sub> , CO, CO <sub>2</sub> and SO <sub>2</sub> tested at 5000 ppm are not poisonous to hydrogen IL-EG sensor (Pt-Ni nanoparticle planar device). (3) CH <sub>4</sub> , CO, CO <sub>2</sub> and SO <sub>2</sub> tested at 5000 ppm are not poisonous to oxygen IL-EG sensor (Pt-Ni nanoparticle planar device) ; (4) For gold planar IL-EG device, water tested at 6% affects IL-EG oxygen sensor but sensitivity and accuracy was shown that can be calibrated in the presence of water. When water is less than 400ppm, interference is negligible.
Telemetry	Possible but Not tested yet
Expected lifetime	tested for 6 months

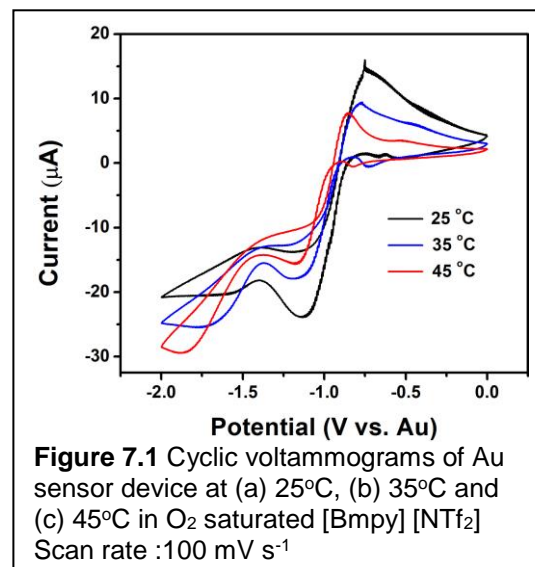
Our Phase I work is shown to establish the proof of concept of our miniaturized and continuous gas sensors that can be a key component for autonomous/self-reporting gas sensor system for a broad range of mine safety and health applications. In the Phase II of this AFC518 project if selected for continuous funding, we will develop and validate a miniaturized, low-cost, low-power, highly reliable, multi-analyte gas sensor system to provide continuous real-time measurements of mine gases with the cost, power consumption, size and ease of use for its adoption and adaptation into mine practice. Our Phase II research plan includes the following objectives: 1) development of a multi-analyte sensor array that measures a large set of target gases (e.g. methane, hydrogen, carbon monoxide, sulfur dioxide, nitrogen dioxide, oxygen) in a single device by strategically integrating multiple sensing modes (e.g. chronoamperometry, electrochemical impedance, piezoelectric quartz crystal microbalance and quartz tuning fork sensing), 2) exclusive use of low-cost batch fabrication manufacturing technologies for a sensor array and integration with miniaturized chip based instrumentation electronics, 3) development of active dust mitigation method in the miniaturized sensor prototype; 4), develop and test gas sampling strategies ( passive vs. active gas sampling strategies) and study the effects of air movement effects on gas sampling on sensor performance; 5) systematic improvements in sensor reliability and autonomous operation in mine environment that will greatly reduce maintenance and training costs and 6) a “plug-in module” approach that minimizes the hardware required for the sensor array systems but still permits great flexibility of use, 7) field test in simulated mines or real mines to validate and benchmark the sensor prototype performance for its adoption and adaption for mine safety practice.

**7.0 Appendices:** In the following sections, we include our work that cannot be easily formatted in the above final report. It includes three sections: 1) on-going work in testing the temperature effects on IL-EG sensor; 2) on-going work in permissible design of sensor in mines; 3) the supporting figures and materials cited for objective 1-3 in section 6.

### 1. Testing temperature effects on IL-EG sensor

In mines, air conditioning systems are often installed at working faces, in road headings or in entire mines to guarantee tolerable climatic conditions. Above an effective temperature of 30°C, working in underground is only allowed under exceptional circumstances and it is completely forbidden at temperatures above 32°C. However, high temperature environment can be encountered in deep underground mines due principally to the geothermal gradient, increasing air pressure from auto-compression of the air column, and groundwater.

Our early work has demonstrated that ILs are excellent sensing materials for high temperature gas sensing (e.g. 120°C) due to their remarkable thermal stability. We designed a chemically selective IL sensor array for the detection and classification of gaseous analytes with pattern recognition at high temperature (120°C) using piezoelectric quartz crystal microbalance (QCM) readout<sup>53-54</sup>. In this project, we have tested the temperature effects for oxygen sensing at 25 °C, 35 °C and 45 °C using our gold planar IL-EG sensor prototype (shown in **Figure 1.1** in section 5). As shown in Figure 7.1, with increasing temperature, the current signals decreased. This is due to the lower solubility, thus lower oxygen concentration in the ILs at higher temperature. The electrochemical impedance study shows that with increase of temperature, the IL electrolyte resistance decreases (90.94  $\Omega$  (25°C), 79.34 $\Omega$  (35°C) and 58.14 $\Omega$  (45°C)). In Objective 2 of this report, we demonstrated that synergistically combining the benefits of non-volatile and conductive ILs with bimetallic nanocatalyst (i.e. Pt-Ni nanosphere) can create unique interface for promoting electron/ion transports to allow highly reproducible, sensitive and selective electrochemical gas sensing in a miniaturized sensor platform. We are currently in the process of characterizing gas sensing properties of the Pt-Ni nanoparticle based microdevice at varying temperatures as nanoparticle based microsensor devices are likely our choices of the final microsensor array prototype. Not only electrode interface areas were maximized by the use of nanomaterial, electrode selectivity can also be improved owing to the unique IL- nanoelectrode interface. As shown in Contact angle experiments in Objective 2 study above, desired wettability of the IL electrolyte on the Pt-Ni NPs suggesting Pt-Ni alloy NPs have balanced hydrophobic/hydrophilic properties. The outstanding gas sensing properties of nanomaterial/IL interface may be attributed to unique surface chemisorption and highly efficient catalytic reaction of gas species of oxygen and hydrogen on the surface of Pt-Ni alloy NPs in the IL. It is expected that temperature and humidity will be factors affect our sensor sensing signals. In our final device that will be developed in Phase II, temperature, humidity and reference sensors will be incorporated in our multimodal sensor array device. These sensors will allow us to calibrate the environmental effects of temperature and humidity and perform quantitative analysis of gas concentrations with high reliability.



## 2. Virtual dust blinds

Dust mitigation is an important issue for sensors installed in coal mines, especially long wall mining. Conventional filters can be quickly clogged by dusts. We plan to design an active dust mitigation method by generating a virtual dust blind in front of the sensor using ultrasonic waves. Specifically, as shown in **Figure 7.2** below, rings of electrodes are fabricated on both sides of a piezoelectric layer (i.e., PZT). Ultrasonic waves will emit from the substrate when sinusoidal voltages are applied to the electrodes, generating a virtual dust blind above by resonance. Dusts are stopped due to the acoustic radiation force, whereas gas molecules such as methane still can pass through. The ultrasound will operate with a frequency above 100 kHz, so that it won't interfere with quartz tuning fork, whose resonant frequency is 32kHz.

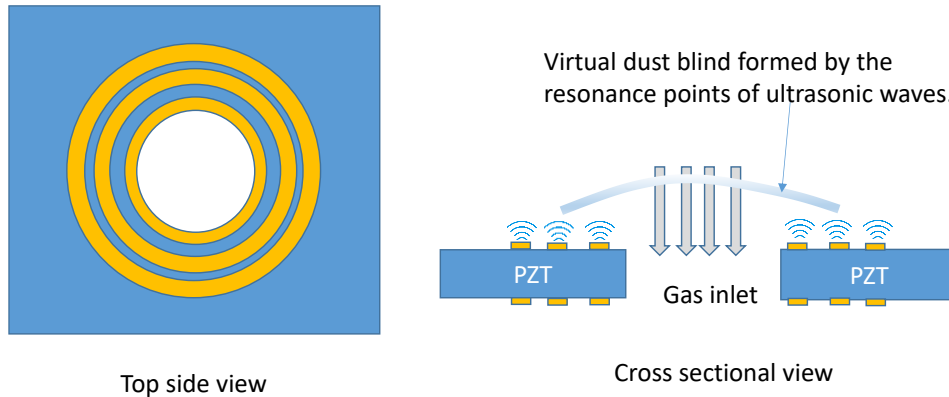


**Figure 7.2. Schematic of a virtual dust blind based on ultrasonic radiation force.**

This approach can be combined with the traditional passive filter method. As shown in **Figure 7.3**, a filter is placed on the top of the active piezoelectric PZT layer. Dust particles, which leak through the ultrasonic blind, will be blocked by the filter. Then the dust particles on the filter can be shaken off by the ultrasonic wave to prevent clogging, analogous to a megasonic cleaner.

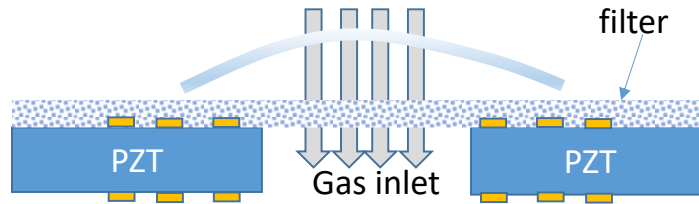


**Figure 7.3. Combination of conventional filter and ultrasonic virtual blind for dust mitigation.**

The cost of this new approach is more power consumption. However, dust mitigation is mainly desirable for long wall applications, for which, the sensor can be stationary and connected to an external power source.

The virtual dust blind based on acoustic radiation force is still at the concept development stage. We were not able to explore this idea further due to the limited resources and time in the phase I project. However, based on our theoretical analysis and literature search, we believe this is a promising approach since acoustic radiation force is well-studied and has already been demonstrated. We are currently simulating the virtual dust blind using COMSOL multiphysics software and next will experimentally investigate this idea by patterning ring electrodes on PZT (Lead zirconate titanate).

### 3. Supporting Figures and Tables for Objective 1-3

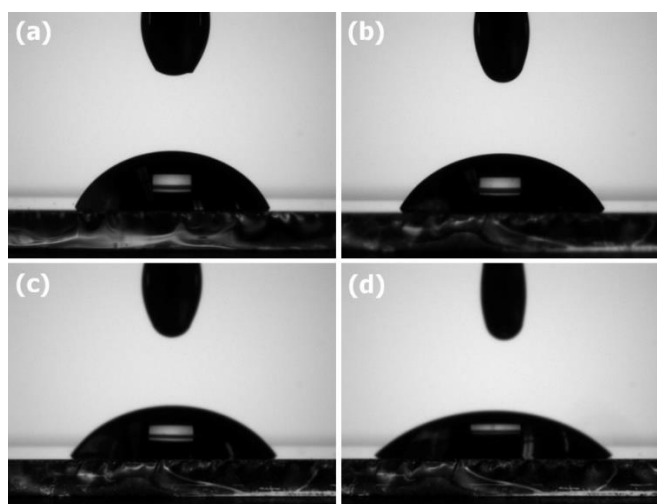


**Figure S1.1.** The contact angle measurement of (a) original IL, (b) IL+2% H<sub>2</sub>O, (c) IL+4% H<sub>2</sub>O and (d) IL+6% H<sub>2</sub>O on the gold coated substrate

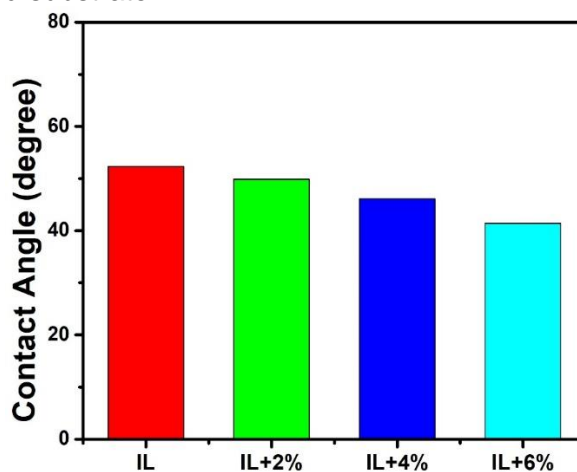


**Figure S1.2.** The contact angle measurement of (a) original IL, (b) IL+2% H<sub>2</sub>O, (c) IL+4% H<sub>2</sub>O and (d) IL+6% H<sub>2</sub>O on the gold substrate.

**Table S1.1.** The comparison of Rs value in N<sub>2</sub> and O<sub>2</sub> saturated ionic liquids

Sample	Rs (N <sub>2</sub> ) /Ω	Rs (O <sub>2</sub> ) /Ω
IL	150.7	183.8
IL+2%	140.6	175.5
IL + 4%	135.2	169.9
IL +6%	129.3	160.2

**Table S1.2.** The reduction peak potential of oxygen to superoxide in the IL with different amount of water electrolytes in **Figure 1.3**

samples	Reduction potential ( $E_{red1}$ ) V (Vs. Au)	Reduction potential ( $E_{red2}$ ) V (Vs. Au)
IL	-1.25 V	-1.61 V
IL+2% H <sub>2</sub> O	-1.12 V	-1.50 V
IL+4% H <sub>2</sub> O	-0.86 V	-1.32 V
IL+6% H <sub>2</sub> O	-0.76 V	-1.24 V

**Table S2.1** Summary results obtained from contact angle measurements

samples	Contact angle (degree)
Bmpy[NTf <sub>2</sub> ]@Pt-Ni/C	38.3
Bmpy[NTf <sub>2</sub> ]@Pt/C	68.2
BmimBF <sub>4</sub> @Pt-Ni/C	53.5

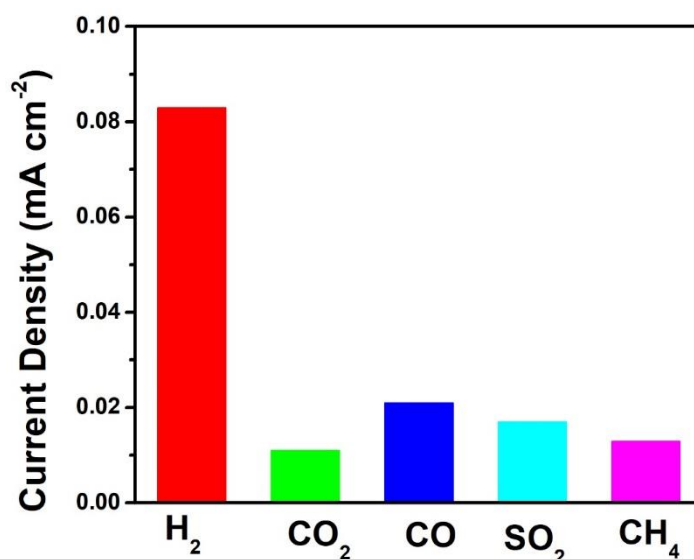


**Figure S2.1.** Selectivity of the Pt-Ni-12h based sensor successive exposure to 500 ppm H<sub>2</sub> vs. to 5000ppm various gases (CO<sub>2</sub>, CO, SO<sub>2</sub> or CH<sub>4</sub>) at room temperature. The current density obtained from chronoamperometry measurement.

## 8.0 Acknowledgement/Disclaimer:

This study was sponsored by the Alpha Foundation for the Improvement of Mine Safety and Health, Inc. (ALPHA FOUNDATION). The views, opinions and recommendations expressed herein are solely those of the authors and do not imply any endorsement by the ALPHA FOUNDATION, its Directors and staff.

## References:

1. Ignat'ev, N.; Welz-Biermann, U.; Kucheryna, A.; Bissky, G.; Willner, H., New ionic liquids with tris (perfluoroalkyl) trifluorophosphate (FAP) anions. *Journal of Fluorine Chemistry* **2005**, 126 (8), 1150-1159.
2. Fitchett, B. D.; Knepp, T. N.; Conboy, J. C., 1-Alkyl-3-methylimidazolium Bis (perfluoroalkylsulfonyl) imide water-immiscible ionic liquids the effect of water on electrochemical and physical properties. *Journal of the Electrochemical Society* **2004**, 151 (7), E219-E225.
3. O'Mahony, A. M.; Silvester, D. S.; Aldous, L.; Hardacre, C.; Compton, R. G., Effect of water on the electrochemical window and potential limits of room-temperature ionic liquids. *Journal of Chemical & Engineering Data* **2008**, 53 (12), 2884-2891.
4. Khan, A.; Gunawan, C. A.; Zhao, C., Oxygen Reduction Reaction in Ionic Liquids: Fundamentals and Applications in Energy and Sensors. *ACS Sustainable Chemistry & Engineering* **2017**, 5 (5), 3698-3715.
5. Pozo-Gonzalo, C.; Torriero, A. A. J.; Forsyth, M.; MacFarlane, D. R.; Howlett, P. C., Redox Chemistry of the Superoxide Ion in a Phosphonium-Based Ionic Liquid in the Presence of Water. *The Journal of Physical Chemistry Letters* **2013**, 4 (11), 1834-1837.
6. Pozo-Gonzalo, C.; Virgilio, C.; Yan, Y.; Howlett, P. C.; Byrne, N.; MacFarlane, D. R.; Forsyth, M., Enhanced performance of phosphonium based ionic liquids towards 4 electrons oxygen reduction reaction upon addition of a weak proton source. *Electrochemistry Communications* **2014**, 38, 24-27.
7. Chi, X.; Tang, Y.; Zeng, X., Electrode Reactions Coupled with Chemical Reactions of Oxygen, Water and Acetaldehyde in an Ionic Liquid: New Approaches for Sensing Volatile Organic Compounds. *Electrochimica Acta* **2016**, 216, 171-180.
8. Islam, M. M.; Okajima, T.; Kojima, S.; Ohsaka, T., Water electrolysis: an excellent approach for the removal of water from ionic liquids. *Chemical Communications* **2008**, (42), 5330-5332.
9. Toussaint, V.; Kühne, E.; Shariati, A.; Peters, C., Solubility measurements of hydrogen in 1-butyl-3-methylimidazolium tetrafluoroborate and the effect of carbon dioxide and a selected catalyst on the hydrogen solubility in the ionic liquid. *The Journal of Chemical Thermodynamics* **2013**, 59, 239-242.
10. Xiong, L.; Barnes, E. O.; Compton, R. G., Amperometric detection of oxygen under humid conditions: The use of a chemically reactive room temperature ionic liquid to 'trap' superoxide ions and ensure a simple one electron reduction. *Sensors and Actuators B: Chemical* **2014**, 200, 157-166.
11. Buzzeo, M. C.; Klymenko, O. V.; Wadhawan, J. D.; Hardacre, C.; Seddon, K. R.; Compton, R. G., Voltammetry of Oxygen in the Room-Temperature Ionic Liquids 1-Ethyl-3-methylimidazolium Bis((trifluoromethyl)sulfonyl)imide and Hexyltriethylammonium Bis((trifluoromethyl)sulfonyl)imide: One-Electron Reduction To Form Superoxide. Steady-State and Transient Behavior in the Same Cyclic Voltammogram Resulting from Widely Different Diffusion Coefficients of Oxygen and Superoxide. *The Journal of Physical Chemistry A* **2003**, 107 (42), 8872-8878.
12. Yu, L.; Huang, Y.; Jin, X.; Mason, A. J.; Zeng, X., Ionic liquid thin layer EQCM explosives sensor. *Sensors and Actuators B: Chemical* **2009**, 140 (2), 363-370.
13. Cammarata, L.; Kazarian, S.; Salter, P.; Welton, T., Molecular states of water in room temperature ionic liquids. *Physical Chemistry Chemical Physics* **2001**, 3 (23), 5192-5200.
14. Fazio, B.; Triolo, A.; Di Marco, G., Local organization of water and its effect on the structural heterogeneities in room-temperature ionic liquid/H<sub>2</sub>O mixtures. *Journal of Raman Spectroscopy: An International Journal for Original Work in all Aspects of Raman Spectroscopy, Including Higher Order Processes, and also Brillouin and Rayleigh Scattering* **2008**, 39 (2), 233-237.
15. Interfacial electrochemistry : theory, experiment, and applications. Więckowski, A., Ed. Marcel Dekker: New York :, 1999.
16. Pfaffenhuber, C.; Gobel, M.; Popovic, J.; Maier, J., Soggy-sand electrolytes: status and perspectives. *Phys. Chem. Chem. Phys.* **2013**, 15 (42), 18318-18335.

17. Shekibi, Y.; Gray-Weale, A.; MacFarlane, D. R.; Hill, A. J.; Forsyth, M., Nanoparticle Enhanced Conductivity in Organic Ionic Plastic Crystals: Space Charge versus Strain Induced Defect Mechanism. *J. Phys. Chem. C* **2007**, *111* (30), 11463-11468.
18. Osawa, M., Surface-enhanced infrared absorption. In *Near-field optics and surface plasmon polaritons*, Springer: 2001; pp 163-187.
19. Tian, Z.-Q.; Ren, B., Adsorption and reaction at electrochemical interfaces as probed by surface-enhanced Raman spectroscopy. *Annu. Rev. Phys. Chem.* **2004**, *55*, 197-229.
20. Campisi, S.; Schiavoni, M.; Chan-Thaw, C.; Villa, A., Untangling the role of the capping agent in nanocatalysis: recent advances and perspectives. *Catalysts* **2016**, *6* (12), 185.
21. Carpenter, M. K.; Moylan, T. E.; Kukreja, R. S.; Atwan, M. H.; Tessema, M. M., Solvothermal Synthesis of Platinum Alloy Nanoparticles for Oxygen Reduction Electrocatalysis. *Journal of the American Chemical Society* **2012**, *134* (20), 8535-8542.
22. Gan, L.; Cui, C.; Heggen, M.; Dionigi, F.; Rudi, S.; Strasser, P., Element-specific anisotropic growth of shaped platinum alloy nanocrystals. *Science* **2014**, *346* (6216), 1502-1506.
23. Cui, C.; Gan, L.; Li, H.-H.; Yu, S.-H.; Heggen, M.; Strasser, P., Octahedral PtNi nanoparticle catalysts: exceptional oxygen reduction activity by tuning the alloy particle surface composition. *Nano letters* **2012**, *12* (11), 5885-5889.
24. Wu, Y.; Wang, D.; Niu, Z.; Chen, P.; Zhou, G.; Li, Y., A strategy for designing a concave Pt–Ni alloy through controllable chemical etching. *Angewandte Chemie* **2012**, *124* (50), 12692-12696.
25. Stamenkovic, V.; Mun, B. S.; Mayrhofer, K. J.; Ross, P. N.; Markovic, N. M.; Rossmeisl, J.; Greeley, J.; Nørskov, J. K., Changing the activity of electrocatalysts for oxygen reduction by tuning the surface electronic structure. *Angewandte Chemie* **2006**, *118* (18), 2963-2967.
26. Greeley, J.; Stephens, I.; Bondarenko, A.; Johansson, T. P.; Hansen, H. A.; Jaramillo, T.; Rossmeisl, J.; Chorkendorff, I.; Nørskov, J. K., Alloys of platinum and early transition metals as oxygen reduction electrocatalysts. *Nature chemistry* **2009**, *1* (7), 552.
27. Lim, B.; Jiang, M.; Camargo, P. H.; Cho, E. C.; Tao, J.; Lu, X.; Zhu, Y.; Xia, Y., Pd-Pt bimetallic nanodendrites with high activity for oxygen reduction. *science* **2009**, *324* (5932), 1302-1305.
28. Snyder, J.; Fujita, T.; Chen, M.; Erlebacher, J., Oxygen reduction in nanoporous metal–ionic liquid composite electrocatalysts. *Nature materials* **2010**, *9* (11), 904.
29. Chen, C.; Kang, Y.; Huo, Z.; Zhu, Z.; Huang, W.; Xin, H. L.; Snyder, J. D.; Li, D.; Herron, J. A.; Mavrikakis, M., Highly crystalline multimetallic nanoframes with three-dimensional electrocatalytic surfaces. *Science* **2014**, *343* (6177), 1339-1343.
30. Mun, B. S.; Watanabe, M.; Rossi, M.; Stamenkovic, V.; Markovic, N. M.; Ross Jr, P. N., A study of electronic structures of Pt 3 M (M= Ti, V, Cr, Fe, Co, Ni) polycrystalline alloys with valence-band photoemission spectroscopy. *The Journal of chemical physics* **2005**, *123* (20), 204717.
31. Nørskov, J. K.; Rossmeisl, J.; Logadottir, A.; Lindqvist, L.; Kitchin, J. R.; Bligaard, T.; Jonsson, H., Origin of the overpotential for oxygen reduction at a fuel-cell cathode. *The Journal of Physical Chemistry B* **2004**, *108* (46), 17886-17892.
32. Godínez-Salomón, F.; Hallen-López, M.; Solorza-Feria, O., Enhanced electroactivity for the oxygen reduction on Ni@ Pt core-shell nanocatalysts. *international journal of hydrogen energy* **2012**, *37* (19), 14902-14910.
33. Gondosiswanto, R.; Hibbert, D. B.; Fang, Y.; Zhao, C., Redox Recycling Amplification Using an Interdigitated Microelectrode Array for Ionic Liquid-Based Oxygen Sensors. *Analytical Chemistry* **2018**, *90* (6), 3950-3957.
34. Hu, C.; Bai, X.; Wang, Y.; Jin, W.; Zhang, X.; Hu, S., Inkjet Printing of Nanoporous Gold Electrode Arrays on Cellulose Membranes for High-Sensitive Paper-Like Electrochemical Oxygen Sensors Using Ionic Liquid Electrolytes. *Analytical Chemistry* **2012**, *84* (8), 3745-3750.
35. Lucio, A. J.; Shaw, S. K., Effects and controls of capacitive hysteresis in ionic liquid electrochemical measurements. *Analyst* **2018**, *143* (20), 4887-4900.
36. Shabir, G. A., Validation of high-performance liquid chromatography methods for pharmaceutical analysis: Understanding the differences and similarities between validation

- requirements of the US Food and Drug Administration, the US Pharmacopeia and the International Conference on Harmonization. *Journal of Chromatography A* **2003**, 987 (1), 57-66.
37. S Bashammakh, A., Extractive spectrophotometric determination of bismuth (III) in water using some ion pairing reagents. *Journal of Chemistry* **2011**, 8 (3), 1462-1471.
  38. Tang, Y.; He, J.; Gao, X.; Yang, T.; Zeng, X., Continuous amperometric hydrogen gas sensing in ionic liquids. *Analyst* **2018**, 143 (17), 4136-4146.
  39. Choi, S.-I.; Xie, S.; Shao, M.; Odell, J. H.; Lu, N.; Peng, H.-C.; Protsailo, L.; Guerrero, S.; Park, J.; Xia, X.; Wang, J.; Kim, M. J.; Xia, Y., Synthesis and Characterization of 9 nm Pt–Ni Octahedra with a Record High Activity of 3.3 A/mgPt for the Oxygen Reduction Reaction. *Nano Letters* **2013**, 13 (7), 3420-3425.
  40. Chen, C.; Kang, Y.; Huo, Z.; Zhu, Z.; Huang, W.; Xin, H. L.; Snyder, J. D.; Li, D.; Herron, J. A.; Mavrikakis, M.; Chi, M.; More, K. L.; Li, Y.; Markovic, N. M.; Somorjai, G. A.; Yang, P.; Stamenkovic, V. R., Highly Crystalline Multimetallic Nanoframes with Three-Dimensional Electrocatalytic Surfaces. *Science* **2014**, 343 (6177), 1339-1343.
  41. Silvester, D. S.; Aldous, L.; Hardacre, C.; Compton, R. G., An Electrochemical Study of the Oxidation of Hydrogen at Platinum Electrodes in Several Room Temperature Ionic Liquids. *The Journal of Physical Chemistry B* **2007**, 111 (18), 5000-5007.
  42. Tang, Y.; Lin, L.; Kumar, A.; Guo, M.; Sevilla, M.; Zeng, X., Hydrogen Electrooxidation in Ionic Liquids Catalyzed by the NTf<sub>2</sub> Radical. *The Journal of Physical Chemistry C* **2017**, 121 (9), 5161-5167.
  43. Wang, Z.; Guo, M.; Baker, G. A.; Stetter, J. R.; Lin, L.; Mason, A. J.; Zeng, X., Methane-oxygen electrochemical coupling in an ionic liquid: a robust sensor for simultaneous quantification. *Analyst* **2014**, 139 (20), 5140-5147.
  44. Friedt, J. M.; Carry, E., Introduction to the quartz tuning fork. *Am J Phys* **2007**, 75 (5), 415-422.
  45. Zeisel, D.; Menzi, H.; Ullrich, L., A precise and robust quartz sensor based on tuning fork technology for (SF<sub>6</sub>)-gas density control. *Sensor Actuat a-Phys* **2000**, 80 (3), 233-236.
  46. Christen, M., Air and Gas Damping of Quartz Tuning Forks. *Sensor Actuator* **1983**, 4 (4), 555-564.
  47. Cashdollar, K. L.; A. Zlochower, I.; Green, G. M.; Thomas, R. A.; Hertzberg, M., Flammability of methane, propane, and hydrogen gases. *Journal of Loss Prevention in the Process Industries* **2000**, 13 (3), 327-340.
  48. Wang, Z.; Mu, X.; Guo, M.; Huang, Y.; Mason, A. J.; Zeng, X., Methane recognition and quantification by differential capacitance at the hydrophobic ionic liquid-electrified metal electrode interface. *Journal of The Electrochemical Society* **2013**, 160 (6), B83-B89.
  49. Wang, Z.; Zeng, X., Bis (trifluoromethylsulfonyl) imide (NTf<sub>2</sub>)-based ionic liquids for facile methane electro-oxidation on Pt. *Journal of The Electrochemical Society* **2013**, 160 (9), H604-H611.
  50. Wang, Z.; Guo, M.; Baker, G. A.; Stetter, J. R.; Lin, L.; Mason, A. J.; Zeng, X., Methane–oxygen electrochemical coupling in an ionic liquid: a robust sensor for simultaneous quantification. *Analyst* **2014**, 139 (20), 5140-5147.
  51. Rehman, A.; Zeng, X., Ionic Liquids as Green Solvents and Electrolytes for Robust Chemical Sensor Development. *Accounts of Chemical Research* **2012**, 45 (10), 1667-1677.
  52. Jin, X.; Yu, L.; Zeng, X., Enhancing the sensitivity of ionic liquid sensors for methane detection with polyaniline template. *Sensors and Actuators B: Chemical* **2008**, 133 (2), 526-532.
  53. Jin, X.; Yu, L.; Garcia, D.; Ren, R. X.; Zeng, X., Ionic Liquid High-Temperature Gas Sensor Array. *Analytical Chemistry* **2006**, 78 (19), 6980-6989.
  54. Yu, L.; Garcia, D.; Ren, R.; Zeng, X., Ionic liquid high temperature gas sensors. *Chemical Communications* **2005**, (17), 2277-2279.